Elastic imaging with exact wavefield extrapolation for application to ocean-bottom 4C seismic data

GEOPHYSICS, VOL. 78, NO. 6 (NOVEMBER-DECEMBER 2013); P. S265–S284, 20 FIGS., 2 TABLES.
10.1190/GEO2013-0152.1

Elastic imaging with exact wavefield extrapolation for application to ocean-bottom 4C seismic data

Matteo Ravasi[1] and Andrew Curtis[1]

ABSTRACT

A central component of imaging methods is receiver-side wavefield backpropagation or extrapolation in which the wavefield from a physical source scattered at any point in the subsurface is estimated from data recorded by receivers located near or at the Earth's surface. Elastic reverse-time migration usually accomplishes wavefield extrapolation by simultaneous reversed-time 'injection' of the particle displacements (or velocities) recorded at each receiver location into a wavefield modeling code. Here, we formulate an exact integral expression based on reciprocity theory that uses a combination of velocity-stress recordings and quadrupole-dipole backpropagating sources, rather than the commonly used approximate formula involving only particle velocity data and dipole backpropagating sources. The latter approximation results in two types of nonphysical waves in the scattered wavefield estimate: First, each arrival contained in the data is injected upward and downward rather than unidirectionally as in the true time-reversed experiment; second, all injected energy emits compressional and shear propagating modes in the model simulation (e.g., if a recorded P-wave is injected, both P and S propagating waves result). These artifacts vanish if the exact wavefield extrapolation integral is used. Finally, we show that such a formula is suitable for extrapolation of ocean-bottom 4C data: Due to the fluid-solid boundary conditions at the seabed, the data recorded in standard surveys are sufficient to perform backpropagation using the exact equations. Synthetic examples provide numerical evidence of the importance of correcting such errors.

INTRODUCTION

Acquisition of the seismic wavefield directly at the seabed provides the only possible direct recordings of shear waves in marine seismics. Modern acquisition systems make use of 4C sensors consisting of a multicomponent geophone and a hydrophone, to record the elastic wavefield in the solid seabed and the acoustic wavefield in the water just above the seabed. They are usually connected to each other by, and are housed within, a so-called *ocean-bottom cable* (OBC), which transmits data to a recording system on a boat using wired telemetry, while a second boat fires a marine source around and over the sensors (Berg et al., 1994; Amal et al., 2005). Alternatively, remotely operated vehicles can be used to deploy individual sensor nodes (ocean-bottom node, OBN) on the seafloor allowing more flexible acquisition geometries (Ronen et al., 2003; Granger et al., 2005). Recording data in this way has certain advantages over conventional marine acquisition where streamers of hydrophones and multicomponent accelerometers are towed behind a vessel. Ocean-bottom seismics can in principle be used to acquire data in areas congested by platforms or other obstacles at the sea surface, to provide wide-azimuth illumination, to improve repeatability, to collect shear-wave (S-wave) as well as acoustic (P-wave) energy, and to provide higher resolution due to the shorter wavelengths of S-waves compared to P-waves (Maver, 2011).

Although the P-wave energy is often easier than S-waves to generate, record, and process in marine seismics, S-waves can provide additional information about the subsurface. Imaging with multicomponent seismic data can better describe the physics of wave propagation, and resulting seismic images more accurately characterize the subsurface (Zhu et al., 1999; Gaiser et al., 2001; Simmons and Backus, 2003; Stewart et al., 2003; Ravasi and Curtis, 2013). Pure-mode (SS) or converted-mode (PS/SP) shear-wave images have many applications: For example, they provide useful information to discriminate gas-related from nonhydrocarbon-related reflection amplitude anomalies (Hughes et al., 2010), image through gas clouds where the P-wave signal is attenuated (Thomsen et al.,

Manuscript received by the Editor 16 April 2013; revised manuscript received 10 July 2013; published online 31 October 2013.
[1]The University of Edinburgh, Grant Institute, School of GeoSciences, Edinburgh, UK. E-mail: M.Ravasi@sms.ed.ac.uk; andrew.curtis@ed.ac.uk.

1997; Knapp et al., 2001), estimate density (Leiceaga et al., 2010), improve the ability to characterize lithology (Shahraeeni and Curtis, 2011; Shahraeeni et al., 2012), and detect fractures (Li, 1998).

Different schemes used for processing ocean-bottom data can be classified by the type of information used at the imaging stage to estimate the subsurface structure. The traditional way is to remove all free-surface multiples and image with only primary reflections (Yilmaz, 1989). A technique known as PZ summation (Barr and Sander, 1989; Soubaras, 1996; Schalkwijk et al., 1999) attenuates strong free-surface multiples by combining the geophone and hydrophone recordings: It exploits the polarity difference between an isotropic measurement (pressure) and a directional measurement (velocity) to eliminate the receiver ghost and the water-column reverberations. A more sophisticated method is to deconvolve the up- and downgoing wavefields (Sonneland and Berg, 1987; Amundsen, 2001; Wang et al., 2009). This provides receiver- and source-side free-surface multiple attenuation but also deghosting and signature deconvolution in layered and complex media, although it puts strict requirements on the spatial density of source and receiver locations. This latter method has the further advantage that it can also be applied to the horizontal components and therefore allows a complete free-surface demultiple method for converted-wave (PS) data.

Alternatively, free-surface multiples (and additionally, internal multiples) can be treated as a useful signal and migrated together with the primaries: Because they are formed by the same source signal as the primaries but travel along different paths through the medium, they contain information not contained in the primaries. Several authors have used the receiver ghost for migration of ocean-bottom data (Godfrey et al., 1998; Ronen et al., 2005; Grion et al., 2007; Dash et al., 2009). Muijs et al. (2007) make an early attempt to image using primary and free-surface multiples together: the final image contains crosstalk artifacts however; they are caused by interference of up- and downgoing waves not associated with the same subsurface reflector. Wong et al. (2010) define a joint, linear least-squares inversion framework that can migrate primary and ghost signals together, combining their structural information free from crosstalk. This method was then modified to account for the subsequent higher order multiples (Wong et al., 2011). Note that all of these techniques require the data to be decomposed into up- and downgoing components.

A distinction may also be made between methods that migrate (or assume the recorded wavefield comprises) only P-waves and those that image using the full elastic wavefield. Two possible avenues exist to make use of the extra elastic wavefield information contained in multicomponent ocean-bottom data at the imaging stage. The first is borrowed from the acoustic case: It uses a purely scalar wave equation for extrapolation. For such methods, wavefield decomposition into scalar and vector potentials is performed before extrapolation; the success of such a separation heavily depends on the estimation of ocean-bottom elastic properties, which is often inaccurate. After separation, up- and downgoing P- and S-wavefields are processed separately as scalar wavefields, using existing processing algorithms (multiple elimination, migration) developed for acoustic wavefields. The main disadvantage of such methods is that the wavefield is treated as purely P or purely S during extrapolation; thus, conversions that may occur during propagation between any image point and the receivers are ignored. The other avenue is to treat data in a vector form and use fully elastic reverse-time migration (RTM) (Chang and McMechan, 1986, 1994; Sun and McMechan, 1986; Yan and Sava, 2008). Particle displacement (or velocity) recordings are usually directly injected as a boundary condition in a numerical solution to the elastic wave equation; the separation into P- and S-waves is then performed just before the imaging condition is applied.

In this paper, a more accurate boundary condition is proposed for wavefield injection, which accounts for velocity and stress or strain recordings. The new method eliminates most of the problems discussed above. We begin by defining an integral framework for elastic imaging derived from source-receiver interferometry (SRI) (Curtis and Halliday, 2010; Halliday and Curtis, 2010; Vasconcelos, 2013). This results in a double-integral approach: A first integral representation is used for extrapolation of the scattered wavefield due to a conceptual, scattering source at any image point (i.e., receiver-side reverse time wavefield extrapolation), while a second integral represents the imaging condition needed to combine the extrapolated source- and receiver-side (recorded) wavefields. First, we review the nonlinear, elastic imaging condition integral that crosscorrelates scalar and/or vector potentials at the image point, discussed more extensively in Ravasi and Curtis (2013). Then we derive an exact wavefield extrapolation integral expression based on reciprocity theory that uses a combination of velocity-stress recordings and quadrupole-dipole backpropagating sources (i.e., it performs *tensorial* wavefield extrapolation). This allows the extrapolation of receiver-side wavefields without the introduction of nonphysical waves that arise when wavefield extrapolation is accomplished by direct injection of particle velocity components at the receiver locations (*vectorial* wavefield extrapolation — Yan and Sava, 2007). Then we discuss how our tensorial wavefield extrapolation integral becomes practical for backpropagation of recorded ocean-bottom 4C data: We show that only particle velocity and pressure recordings are required over the available portion of the seabed because of the incorporation of the physical boundary conditions that govern the fluid-solid boundary. Numerical examples are used to illustrate the advantages of tensorial wavefield extrapolation over common-practice vectorial extrapolation.

SRI-BASED ELASTIC IMAGING

The acoustic nonlinear, reverse-time imaging approach proposed by Halliday and Curtis (2010) and Vasconcelos (2011, 2013), which is suitable for marine seismic data acquisition of vector-acoustic data, is based on the so-called source-receiver interferometry or SRI theory (Curtis and Halliday, 2010). Because SRI is derived for acoustic and elastic media by Curtis and Halliday (2010), the corresponding imaging methods can also be extended to elastic media and thus made suitable for alternative data acquisition systems. A particular case is marine seismic acquisition of ocean-bottom data, and another is the related case of land seismic acquisition, both of which require an elastic formulation to account for recorded shear energy. We now review previous aspects of this formulation and extend it as required for exact elastic wavefield extrapolation and for imaging.

Our ocean-bottom formulation is based on source-receiver scattering reciprocity relations, for wavefield extrapolation and for the imaging condition. It can be used with data from an acquisition geometry similar to that depicted in Figure 1a, where sources are towed below the sea-air interface (free surface), receivers are placed on the seabed, and we imagine a further source and receiver

at each point at which we wish to create an image in the subsurface. This configuration is regarded as an incomplete approximation to the ideal "complete" geometry conceptualized in Figure 1b. The latter is composed of a physical boundary of sources that surrounds a physical boundary of receivers and the imaginary source and receiver colocated in the subsurface domain. This is one of three canonical geometries for the theory of SRI (Curtis and Halliday, 2010; Halliday and Curtis, 2010), the theory we draw from in what follows.

When acquiring data using OBCs, receivers are usually densely and uniformly distributed, at least along the inline direction. Otherwise, if OBNs are preferred, receivers are coarsely and nonuniformly located. In both cases, but especially in the latter, data must be interpolated onto a uniform grid before they can be injected without aliasing in any standard finite-difference code for imaging purposes. To overcome this limitation, imaging can be performed by first applying source-receiver reciprocity: Seismic data can instead be injected simultaneously along the well-sampled boundary of sources (i.e., treating this boundary as if using it for receiver-side wavefield extrapolation), while the source wavelet is injected at any individual receiver location (treating each receiver as if it was a source and injecting the source-side wavefield). Such a reciprocal source-receiver formulation is proposed in Appendix A, and in the main text, we present the more usual formulation.

Elastic imaging conditions

Ravasi and Curtis (2013) use inter-receiver elastic wavefield interferometry and follow a similar type of derivation to the acoustic work of Fleury and Vasconcelos (2012) to derive a nonlinear, elastic, reciprocity-based, frequency-domain imaging condition that is suitable for imaging of ocean-bottom or land data (Figure 2a):

$$
\begin{aligned}
I^{nl}_{NM}(\mathbf{x}) &= 2\mathrm{Re}\{G^{S(\Phi,\Phi)}_{(M,N)}(\mathbf{x}, t=0)\} \\
&= -\int\Bigg(\int_{\partial V_S}(\bar{G}^{S(\Phi,h)}_{(M,ij)}(\mathbf{x},\mathbf{x}_S)\{G^{0(\Phi,f)}_{(N,i)}(\mathbf{x},\mathbf{x}_S)\}^* \\
&\quad + \bar{G}^{S(\Phi,f)}_{(M,i)}(\mathbf{x},\mathbf{x}_S)\{G^{0(\Phi,h)}_{(N,ij)}(\mathbf{x},\mathbf{x}_S)\}^*)n_{S_j}d\mathbf{x}_S\Bigg)d\omega \\
&\quad - \int\Bigg(\int_{\partial V_S}(\bar{G}^{(\Phi,h)}_{(M,ij)}(\mathbf{x},\mathbf{x}_S)\{G^{S(\Phi,f)}_{(N,i)}(\mathbf{x},\mathbf{x}_S)\}^* \\
&\quad + \bar{G}^{(\Phi,f)}_{(M,i)}(\mathbf{x},\mathbf{x}_S)\{G^{S(\Phi,h)}_{(N,ij)}(\mathbf{x},\mathbf{x}_S)\}^*)n_{S_j}d\mathbf{x}_S\Bigg)d\omega, \quad (1)
\end{aligned}
$$

where the two superscripts between brackets on the G terms represent the observed quantity and the source type, respectively, and the subscripts identify the selected *components* (similar to the notation of Wapenaar and Fokkema, 2006). Here, superscripts Φ refer to potentials and are associated with subscript capital letters M and N, each of which can be substituted by P or S_k with component $k = 1, 2, 3$ to identify P- or S-wave virtual receivers in the subsurface. Superscripts f and h represent external volume force (dipole) sources and external deformation rate (quadrupole) sources, respectively, while subscripts i/ij identify the i-th/ij-th component of the external volume force vectors and external deformation rate tensors. A further superscript $0/S$ is added to discriminate the reference/scattered Green's function from the full Green's function, respectively, where the full Green's function is $G = G^0 + G^S$ and G^0 is the Green's function calculated through a prior

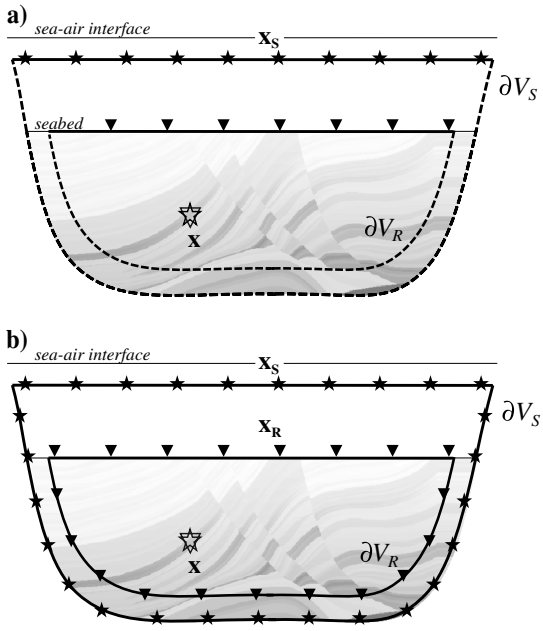

Figure 1. (a) Acquisition geometry used to formulate a SRI framework for nonlinear, reverse-time imaging of elastic ocean-bottom data. Sources (stars) are towed below the sea-air interface, and receivers (triangles) are placed at the seabed. (b) Conceptualization of a complete acquisition geometry to which that in (a) is an approximation.

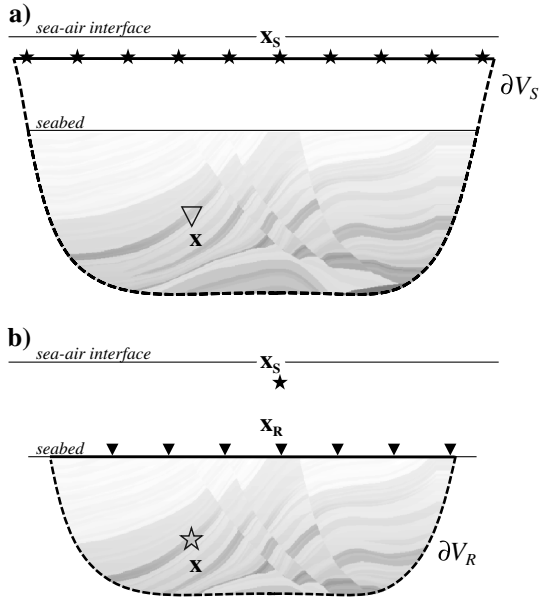

Figure 2. Geometries used for the reciprocity-based imaging condition and wavefield extrapolation. (a) At the imaging stage, a closed, discretized source boundary ∂V_S surrounds two imaginary colocated receivers at the image point $\mathbf{x}$ in the subsurface. (b) At the backpropagation stage, a closed receiver boundary ∂V_R surrounds an imaginary source at the image point $\mathbf{x}$ in the subsurface, while the physical source $\mathbf{x_S}$ is located outside of ∂V_R. Sources and receivers actually used in usual acquisition scenarios are represented by stars and triangles, respectively.

estimate of the subsurface velocity model. Extrapolated Green's functions (so-called receiver-side wavefields) are represented as $\bar{G}$ to differentiate them from forward modeled Green's functions (so-called source-side wavefields). For example, the Green's function $\bar{G}^{S(\Phi,f)}_{(N,i)}(\mathbf{x},\mathbf{x}_S)$ is the scattered P or S extrapolated wavefield that would be recorded at location $\mathbf{x}$ due to a point force source excited along the ith direction at $\mathbf{x}_S$. Finally, n_{S_j} is the j-th component of the normal vector $\mathbf{n}_S$ on the boundary of sources ∂V_S and ω is the angular frequency. Note that Einstein's summation convention for repeated indices is used throughout this paper. Notice also that all terms inside the integral consist of one wavefield multiplied by the complex conjugate (*) of another, which corresponds to cross-correlation in the time domain; this is also true of all integrals presented below. For the reader's convenience, in Table 1 we define a list of variables that we use in this paper.

The image $I^{nl}_{NM}(\mathbf{x})$ on the left of equation 1 is composed of a first term that focuses single-scattered energy at the image point $\mathbf{x}$ and a second term that accounts for nonlinear interactions between the wavefield and the model. Ravasi and Curtis (2013) show that $I^{nl}_{NM}(\mathbf{x})$ in fact represents the zero-time sample of the Green's function $G^{S(\Phi,\Phi)}_{(M,N)}(\mathbf{x},t)$ at $\mathbf{x}$: that is, the received scattered P- or S-wave (M) recorded at point $\mathbf{x}$, due to a P- or S-wave source (N) also located at $\mathbf{x}$. This will only be nonzero if there is a perturbation of the background medium exactly at $\mathbf{x}$. Hence, this zero-time value is a good candidate to be used as an imaging condition.

Because the formulation with unidirectional point force sources is not practical for marine ocean-bottom applications, the transformation that Wapenaar and Fokkema (2006) propose is used to change source quantities on ∂V_S to be P- and S-wave sources. Assuming that the medium at, and outside of, ∂V_S is homogeneous, isotropic, and unperturbed (i.e., waves only propagate inward from the source boundary ∂V_S due directly to the source at $\mathbf{x}_S$, and are not scattered back inward by external heterogeneities), a shot-profile imaging condition with monopole/dipole P- and S-wave sources is given by

$$\begin{aligned} I^{nl}_{NM}(\mathbf{x}) &= 2\mathrm{Re}\{G^{S(\Phi,\Phi)}_{(M,N)}(\mathbf{x},t=0)\} \\ &= \int\left(\frac{2}{j\omega\rho}\int_{\partial V_S}\{\partial_{S_j}\bar{G}^{S(\Phi,\Phi)}_{(M,K)}(\mathbf{x},\mathbf{x}_S)\}^* G^{0(\Phi,\Phi)}_{(N,K)}(\mathbf{x},\mathbf{x}_S)n_{S_j}d\mathbf{x}_S\right)d\omega \\ &\quad + \int\left(\frac{2}{j\omega\rho}\int_{\partial V_S}\{\partial_{S_j}\bar{G}^{(\Phi,\Phi)}_{(M,K)}(\mathbf{x},\mathbf{x}_S)\}^* G^{S(\Phi,\Phi)}_{(N,K)}(\mathbf{x},\mathbf{x}_S)n_{S_j}d\mathbf{x}_S\right)d\omega. \end{aligned} \tag{2}$$

Note that if the above assumption is not satisfied, for example, when source-side ghost and higher order multiples are not previously attenuated from the data, the final image will contain artifacts due to these events. Otherwise, the imaging condition in equation 2 is equivalent to that in equation 1.

This equation still requires the availability of monopole and dipole P- and S-wave source responses: If only monopole P-wave sources are available, S-wave sources must be neglected in equation 2 and the P-wave dipole response can be approximated using $\partial_{S_j}G^{S(\Phi,\Phi)}_{(M,P)}n_{S_j} \approx -(j\omega/c_P)G^{S(\Phi,\Phi)}_{(M,P)}$ (the far-field radiation condition), where c_P is the P-wave velocity (Wapenaar and Fokkema, 2006). Thus, we obtain

$$\begin{aligned} I^{nl}_{NM}(\mathbf{x}) &= 2\mathrm{Re}\{G^{S(\Phi,\Phi)}_{(M,N)}(\mathbf{x},t=0)\} \\ &\approx \frac{2}{\rho c_P}\int\left(\int_{\partial V_S}\{\bar{G}^{S(\Phi,\Phi)}_{(M,P)}(\mathbf{x},\mathbf{x}_S)\}^* G^{0(\Phi,\Phi)}_{(N,P)}(\mathbf{x},\mathbf{x}_S)d\mathbf{x}_S\right)d\omega \\ &\quad + \frac{2}{\rho c_P}\int\left(\int_{\partial V_S}\{\bar{G}^{(\Phi,\Phi)}_{(M,P)}(\mathbf{x},\mathbf{x}_S)\}^* G^{S(\Phi,\Phi)}_{(N,P)}(\mathbf{x},\mathbf{x}_S)d\mathbf{x}_S\right)d\omega. \end{aligned} \tag{3}$$

For the purpose of elastic RTM (i.e., the mapping of unknown subsurface discontinuities using primary reflections), the second term on the right-hand side is almost always neglected because predicting or modeling the scattered source-side wavefield relies on knowledge of subsurface parameters with high spatial resolution, which is seldom available at this stage of seismic imaging. A linearized imaging condition is therefore usually used:

$$\begin{aligned} I^{l}_{NM}(\mathbf{x}) &= 2\mathrm{Re}\{G^{S(\Phi,\Phi)}_{(M,N)}(\mathbf{x},t=0)\} \\ &\approx \frac{2}{\rho c_P}\int\left(\int_{\partial V_S}\{\bar{G}^{S(\Phi,\Phi)}_{(M,P)}(\mathbf{x},\mathbf{x}_S)\}^* G^{0(\Phi,\Phi)}_{(N,P)}(\mathbf{x},\mathbf{x}_S)d\mathbf{x}_S\right)d\omega. \end{aligned} \tag{4}$$

Other than the term $2/\rho c_P$ in front of the integral, this is exactly the imaging condition defined heuristically by Yan and Sava (2008); it is used in the examples below to compare with the elastic PP and PS images created using our new wavefield extrapolation formula presented below.

Table 1. Variable names and definitions.

Name	Definition	Name	Definition
$\mathbf{x}$	Image point position	t	Time
$\mathbf{x}_S$	Source position	$\mathbf{x}_R$	Receiver position
$\mathbf{n}_S$	Source boundary normal vector	$\mathbf{n}_R$	Receiver boundary normal vector
ρ	Density	c_P	P-wave velocity
c_{ijkl}	Compliance	s_{ijkl}	Stiffness
I^l	Linear seismic image	I^{nl}	Nonlinear seismic image
v	Velocity recording	τ	Stress recording
f	External volume force (dipole) source	h	External deformation rate (quadrupole) source
$\mathbf{\Phi}$	Potential recording	p	Pressure recording

Elastic wavefield extrapolation

To evaluate any imaging condition, source and receiver wavefields must first be computed. Although the source-side wavefields $G^{0(\Phi,\Phi)}_{(N,P)}(\mathbf{x},\mathbf{x}_S)$ are easily obtained by forward modeling using the reference model of the subsurface and the survey's known acquisition geometry (usually, a P-wave source and vector potential "receivers" in the subsurface), the receiver-side scattered wavefields $\bar{G}^{S(\Phi,\Phi)}_{(M,P)}(\mathbf{x},\mathbf{x}_S)$ extrapolated to point $\mathbf{x}$ are not directly available. An accurate estimate of this wavefield is fundamental for the creation of an image without artifacts. This estimate is obtained by extrapolating the physically recorded data, given by P-wave sources towed below the sea-air free-surface interface at position $\mathbf{x}_S$ and observed at all available receiver locations $\mathbf{x}_R$ along the seabed, backward in time to any desired subseabed image point $\mathbf{x}$ (Figure 2b). Divergence and curl operators are then applied to the extrapolated wavefields to extract P- and S-waves in the subsurface.

In accord with the theory of source-receiver imaging that Halliday and Curtis (2010) propose, we now provide an exact integral expression for wavefield extrapolation in the form of boundary integrals controlled by recorded elastic data. This reciprocity-based wavefield extrapolation, combined with the imaging condition that Ravasi and Curtis (2013) propose, for the first time provides a theoretically exact source-receiver integral framework for imaging of land or ocean-bottom elastic data. This provides the basis for studies of new acquisition designs because it defines precisely the information that any proposed survey design would and would not provide about any image point in the subsurface.

As derived in Appendix B, an exact integral expression for elastic receiver-side extrapolation with monopole sources and velocity-stress receivers is given by

$$\begin{aligned}\bar{G}^{S(\Phi,\Phi)}_{(M,K)}(\mathbf{x},\mathbf{x}_S) = &-\int_{\partial V_R}(G^{S(\tau,\Phi)}_{(ij,K)}(\mathbf{x}_R,\mathbf{x}_S)\{G^{0(\Phi,f)}_{(M,i)}(\mathbf{x},\mathbf{x}_R)\}^*\\ &+G^{S(v,\Phi)}_{(i,K)}(\mathbf{x}_R,\mathbf{x}_S)\{G^{0(\Phi,h)}_{(M,ij)}(\mathbf{x},\mathbf{x}_R)\}^*)n_{R,j}d\mathbf{x}_R\\ &-\int_{\partial V_R}(G^{(\tau,\Phi)}_{(ij,K)}(\mathbf{x}_R,\mathbf{x}_S)\{G^{S(\Phi,f)}_{(M,i)}(\mathbf{x},\mathbf{x}_R)\}^*\\ &+G^{(v,\Phi)}_{(i,K)}(\mathbf{x}_R,\mathbf{x}_S)\{G^{S(\Phi,h)}_{(M,ij)}(\mathbf{x},\mathbf{x}_R)\}^*)n_{R,j}d\mathbf{x}_R,\end{aligned} \tag{5}$$

where superscripts v,τ represent particle velocity and stress recordings and subscripts i/ij identify the ith/ijth component of the particle velocity vectors and stress tensors, respectively. The subscript K can be replaced by P when only P-wave sources are used in the physical (e.g., marine seismic) experiment:

$$\begin{aligned}\bar{G}^{S(\Phi,\Phi)}_{(M,P)}(\mathbf{x},\mathbf{x}_S) = &-\int_{\partial V_R}(G^{S(\tau,\Phi)}_{(ij,P)}(\mathbf{x}_R,\mathbf{x}_S)\{G^{0(\Phi,f)}_{(M,i)}(\mathbf{x},\mathbf{x}_R)\}^*\\ &+G^{S(v,\Phi)}_{(i,P)}(\mathbf{x}_R,\mathbf{x}_S)\{G^{0(\Phi,h)}_{(M,ij)}(\mathbf{x},\mathbf{x}_R)\}^*)n_{R,j}d\mathbf{x}_R\\ &-\int_{\partial V_R}(G^{(\tau,\Phi)}_{(ij,P)}(\mathbf{x}_R,\mathbf{x}_S)\{G^{S(\Phi,f)}_{(M,i)}(\mathbf{x},\mathbf{x}_R)\}^*\\ &+G^{(v,\Phi)}_{(i,P)}(\mathbf{x}_R,\mathbf{x}_S)\{G^{S(\Phi,h)}_{(M,ij)}(\mathbf{x},\mathbf{x}_R)\}^*)n_{R,j}d\mathbf{x}_R.\end{aligned} \tag{6}$$

A linearized expression for Born imaging is obtained by discarding the terms describing nonlinear interaction between the recorded data and the scattered backpropagators (second line of equation 6), because these require velocity/density models with high spatial resolution to be computed in advance of imaging, which is usually not possible:

$$\begin{aligned}\bar{G}^{S(\Phi,\Phi)}_{(M,P)}(\mathbf{x},\mathbf{x}_S) \approx -\int_{\partial V_R}&(G^{S(\tau,\Phi)}_{(ij,P)}(\mathbf{x}_R,\mathbf{x}_S)\{G^{0(\Phi,f)}_{(M,i)}(\mathbf{x},\mathbf{x}_R)\}^*\\ &+G^{S(v,\Phi)}_{(i,P)}(\mathbf{x}_R,\mathbf{x}_S)\{G^{0(\Phi,h)}_{(M,ij)}(\mathbf{x},\mathbf{x}_R)\}^*)n_{R,j}d\mathbf{x}_R.\end{aligned} \tag{7}$$

The evaluation of this integral expression requires and uses knowledge of particle velocity v in $G^{S(v,\Phi)}_{(i,P)}(\mathbf{x}_R,\mathbf{x}_S)$ and the stress tensor τ in $G^{S(\tau,\Phi)}_{(ij,P)}(\mathbf{x}_R,\mathbf{x}_S)$ at the receiver locations (hence we call this "tensorial" wavefield extrapolation). These recordings are injected separately into the reference medium, respectively, as deformation rate density sources in $G^{0(\Phi,h)}_{(M,ij)}(\mathbf{x},\mathbf{x}_R)$ (the h backpropagator) and volume force density sources in $G^{0(\Phi,f)}_{(M,i)}(\mathbf{x},\mathbf{x}_R)$ (the f backpropagator). Finally, the results are summed together. Note that physical sources of such types are not required (see below): They must only be implemented numerically in the elastic modeling code used for extrapolation.

The main limitation at this point is the requirement that the stress tensor is known along the receiver boundary. When dense arrays of velocity receivers are available (e.g., on land), spatial derivatives of velocity can be calculated, approximating temporal derivatives of strain (Robertsson and Muyzert, 1999). If near-surface material properties can be estimated accurately it is conceivable to estimate stress from strain (e.g., Curtis and Robertsson, 2002; Robertsson and Curtis, 2002). However, in current practice, only particle velocity data are used (stress is ignored). Velocity data are then directly injected as a boundary condition at receiver locations ("vectorial" wavefield extrapolation). This procedure can be expressed in an integral form as

$$\bar{G}^{S(\Phi,\Phi)}_{(M,P)}(\mathbf{x},\mathbf{x}_S) \approx -\int_{\partial V_R} G^{S(v,\Phi)}_{(i,P)}(\mathbf{x}_R,\mathbf{x}_S)\{G^{0(\Phi,f)}_{(M,i)}(\mathbf{x},\mathbf{x}_R)\}^* d\mathbf{x}_R. \tag{8}$$

Equation 8 reveals the simplified nature of common-practice wavefield extrapolation with respect to the exact expression in equation 5, the best-case nonlinear expression in equation 6, and linearized expression in equation 7, all of which employ the full velocity-stress information in elastic waves.

Such a formula (equation 8) is not really an approximation to the exact extrapolation integrals. Rather, it is a heuristic scheme used to estimate the receiver wavefield, which contradicts the theory of reciprocity. Thus, in spite of being kinematically correct, it does not effectively represent the scattered Green's function between a physical source $\mathbf{x}_S$ and any image point $\mathbf{x}$ at all. This results in two types of nonphysical waves: First, during backpropagation each arrival contained in the data is injected upward and downward rather than only downward as in the true time-reversed experiment. Second, all injected energy emits compressional and shear propagating modes (e.g., even if only a recorded P-wave is injected, P and S

propagating modes result and are backpropagated to any image point $\mathbf{x}$).

Application to ocean-bottom 4C data

At first glance, our tensorial wavefield extrapolation integral seems not to be suitable for practical applications because it requires additional information, such as stress recordings, which are not easily available. However, we now show that this method is applicable to ocean-bottom seismic acquisition systems that use 4C sensors to measure the fluid's pressure $p(\mathbf{x}_R, t)$ and the solid's particle displacement vector $\mathbf{u}(\mathbf{x}_R, t)$ (or velocity vector $\mathbf{v}(\mathbf{x}_R, t)$) at the seabed. In fact, under the assumption that the seabed can be approximately defined as a horizontal interface ($\mathbf{n} = \mathbf{i_z}$) between the fluid and solid layers as in Figure 3 (although a similar derivation can be obtained for any shape of seabed), only knowledge of the scattered particle velocity vector and the scattered vertical traction vector is required to perform tensorial wavefield extrapolation (equations 6 and 7):

$$\mathbf{v}(\mathbf{x}_R, t) = \begin{pmatrix} v_x(\mathbf{x}_R, t) \\ v_y(\mathbf{x}_R, t) \\ v_z(\mathbf{x}_R, t) \end{pmatrix}, \quad \mathbf{t_z}(\mathbf{x}_R, t) = \begin{pmatrix} \tau_{xz}(\mathbf{x}_R, t) \\ \tau_{yz}(\mathbf{x}_R, t) \\ \tau_{zz}(\mathbf{x}_R, t) \end{pmatrix}. \quad (9)$$

The boundary condition at the fluid–solid interface dictates (1) continuity of the normal component of particle displacement, (2) the normal component of the traction in the solid equals the negative of the acoustic pressure in the fluid, and (3) the tangential components of the traction in the solid vanish. These constraints result in the following conditions:

$$\begin{aligned} \tau_{xz}(\mathbf{x}_R, t) &= 0, \\ \tau_{yz}(\mathbf{x}_R, t) &= 0, \\ \tau_{zz}(\mathbf{x}_R, t) &= -p(\mathbf{x}_R, t). \end{aligned} \quad (10)$$

Assuming that the scattered component of the recorded wavefields can be extracted from the original recordings, 4C data therefore provide all information needed for the implementation of equation 6, which we can restate using only the data that are usually recorded on existing seabed systems:

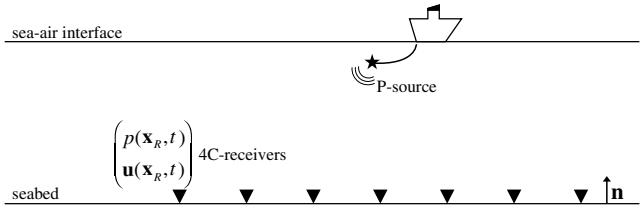

Figure 3. Acquisition of ocean-bottom 4C data. Four-component sensors, consisting of a multicomponent geophone and a hydrophone, are placed along the seabed to record the full elastic wavefield. A boat moves over the sea surface, firing a compressional source at regular intervals. The sea-air interface generates source and receiver ghosts and higher order waterborne multiples. The seabed (liquid-solid interface) is responsible for the conversion process arising when an incident P-wave is transmitted, reflected, and converted into a shear wave.

$$\begin{aligned} \bar{G}^{S(\Phi,\Phi)}_{(M,P)}(\mathbf{x}, \mathbf{x}_S) = &\int_{\partial V_R} (p^S(\mathbf{x}_R, \mathbf{x}_S)\{G^{0(\Phi,f)}_{(M,z)}(\mathbf{x}, \mathbf{x}_R)\}^* \\ &- v^S_z(\mathbf{x}_R, \mathbf{x}_S)\{G^{0(\Phi,h)}_{(M,zz)}(\mathbf{x}, \mathbf{x}_R)\}^*) d\mathbf{x}_R \\ &+ \int_{\partial V_R} (p(\mathbf{x}_R, \mathbf{x}_S)\{G^{S(\Phi,f)}_{(M,z)}(\mathbf{x}, \mathbf{x}_R)\}^* \\ &- v_z(\mathbf{x}_R, \mathbf{x}_S)\{G^{S(\Phi,h)}_{(M,zz)}(\mathbf{x}, \mathbf{x}_R)\}^*) d\mathbf{x}_R. \end{aligned} \quad (11)$$

Thus, provided the fluid-solid boundary conditions hold at the seabed (at least in cases with a lithified seabed capable of supporting shear stress), all of the above results and learning pertains to standard seabed 4C sensors. In what follows, we provide examples that illustrate these points, and which thus demonstrate the advantages of tensorial extrapolation over vectorial extrapolation.

EXAMPLES

Elastic RTM of a single scatterer

Consider a single point scatterer embedded in a constant background medium ($v_P = 2600$ m/s, $v_S = 1400$ m/s, and $\rho = 1000$ kg/m^3) at position $\mathbf{x}_{\text{scatt}} = (1000, 600)$ m. A density perturbation of $\Delta\rho = 600$ kg/m^3 is defined in the otherwise homogeneous density model (Figure 4), and an absorbing boundary condition is applied at the top of the model to prevent the construction of free-surface multiples. Such data are usually referred to as *Born data*; in practice, such data are the result of preprocessing steps that suppress source-side ghosts, receiver-side ghosts, and multiple scattering in the recorded data. A physical compressional source is fired at $\mathbf{x}_S = (1400, 50)$ m, and a horizontal array of receivers is placed at $z_R = 300$ m with inter-receiver spacing of $\Delta x_R = 2$ m. The direct arrival G^0 is subtracted from the recorded data G at each receiver location to give scattered fields $G^{S(v,\Phi)}_{(i,P)}(\mathbf{x}_R, \mathbf{x}_S)$ and $G^{S(\tau,\Phi)}_{(ij,P)}(\mathbf{x}_R, \mathbf{x}_S)$ only. The reference field and the full (reference plus scattered) field are computed using a 2D staggered grid elastic finite-difference algorithm (Virieux, 1986).

Particle velocity recordings are then injected along the receiver array, and the wavefield back-propagation procedure is carried out according to equation 8 using the homogeneous density model as the reference medium for wave propagation. Scalar and vector potentials may be recorded at any image point and crosscorrelated with the source wavefield potentials as required by the linearized imaging condition in equation 4. The receiver-side wavefield is then also estimated using the more accurate tensorial wavefield extrapolator (equation 7), and the same linearized imaging condition is used to produce a second set of elastic images.

PP imaging

Figure 5 shows a series of snapshots of estimated scattered P-wavefields next to the modeled scattered P-wave wavefield $\bar{G}^{S(\Phi,\Phi)}_{(P,P)}(\mathbf{x}, \mathbf{x}_S)$. Note that although the extrapolation calculation is always carried out in reverse time, we prefer to show the wavefields according to the true propagation time in the field experiment. The left plots would (and can) be obtained exactly with a full boundary of receivers (Figure 1b) plus nonlinear tensorial extrapolation in equation 6. The middle column of plots is compromised by data

only being recorded on part of the receiver boundary and by the use of the linearized tensorial extrapolation (equation 7) — in other words, by the one-sided illumination of the subsurface and by knowledge of only the background velocity model as is usually the case in seismic imaging. The right plots are further compromised by using the usual vectorial extrapolator (equation 8). Comparing these plots, only the upper part of the extrapolated wavefields is obtained in seismic extrapolation because the receiver array is only available at the seabed, rather than being an ideal enclosing array as in Figure 1b. In addition, the use of only particle velocity measurements in the usual erroneous method of wavefield extrapolation in the right plots causes two types of nonphysical energy: 1) pervasive injection of down- and upgoing waves at the receiver arrays and 2) a second circular waveform that will collapse at the receiver array after the physical upgoing wave collapses. Both of these features create nonphysical wavefields at image points.

Nonphysical energy of type 1 is the same artifact that arises in the acoustic case when pressure recordings are used for wavefield extrapolation rather than the full vector acoustic (pressure plus particle velocity) data — see Vasconcelos (2013). Nonphysical energy of type 2 is peculiar to the elastic case and is due to injection in the model of the velocity displacement recordings through volume force sources; this emits *both* P- and S-wave propagating modes for each individual P- *or* S-wave arrival (Yan and Sava, 2007). In this specific case, S-wave energy, as is present in the particle velocity recordings, is erroneously injected as P-wave energy along the receiver array, causing the second circular wave in the right plots of Figure 5.

Tensorial versus vectorial wavefield extrapolation integrals analysis.—We now compare the tensorial integral expression for wavefield backpropagation of elastic Born data (equation 7) with the commonly used vectorial version (equation 8), and support an explanation of the nature of nonphysical waves arising in the latter. We borrow the stationary-phase approach (Snieder, 2004) commonly used to analyze seismic interferometry: This approach highlights where, along the receiver boundary ∂V_R, the recorded data and the backpropagators interfere constructively and contribute to the creation of either physical or nonphysical waves in the receiver-side extrapolated wavefield. Associated boundary receivers are called *stationary receivers*.

The single point-scatterer example allows for the identification of three different regions of the subsurface domain (Figure 5): Region A is located above the receiver array ($z \leq z_R$), region B is bounded between the receiver array and the scatterer ($z_R < z \leq z_{\text{scatt}}$), while region C is located below the scatterer depth ($z > z_{\text{scatt}}$). Although the receiver boundary is incomplete and the crosscorrelation between the full recorded data and the scattered receiver propagator (the second line of equation 6, which is nonlinear with respect to the scattered wavefield) is not performed, the tensorial wavefield backpropagation of elastic data generates an almost correct receiver wavefield in the region between the receiver boundary and the scatterer. The stationary point on the receiver array that is needed to construct the scattered P-wave between the physical source and $\mathbf{x}$ is, in fact, located on the available portion of the receiver boundary. The corresponding wavefield is constructed by crosscorrelating the scattered recorded data and the reference receiver propagator (equation 7). However, when components of the stress tensor used for the evaluation of equation 7 (terms with superscript ij) are substituted (approximated) by the "corresponding" components of the particle velocity vector (equation 8), the receiver wavefield shows two nonphysical waves above the receiver line and another nonphysical event below the scatterer.

Nonphysical event 1 (indicated in Figure 5) arises when the scattered P-wave reaches the receiver array; it is also backpropagated (erroneously) upward. Such an artifact therefore occurs only in the portion of the model above the receiver array in this case, due to the absorbing boundary condition at the top of the model. Given a generic point $\mathbf{x}_A$ in region A, this backpropagated wave reaches that location at a time equal to the time that would be obtained by effectively crosscorrelating the P-wave scattered data $G^{S(\Phi,\Phi)}_{(P,P)}(\mathbf{x}_R,\mathbf{x}_S)$ and the P-wave reference propagator $G^{0(\Phi,\Phi)}_{(P,P)}(\mathbf{x}_A,\mathbf{x}_R)$; because crosscorrelation subtracts the phase of one wavefield from another, the arrival time of the erroneous wavefield is the difference between the traveltimes of the two correlated wavefields (Figure 6a). An explanation of the symmetry between the backpropagation path and the physical one with respect to the receiver array comes from the fact that all the recorded energy focuses at two subsurface points, the first being at the actual scatterer location and the second being the symmetric reflection of that location through the receiver array (see Figure 5c — time 2). The same analysis can be carried out for any point contained in the gray cone in Figure 6a to identify first the corresponding stationary receiver and also the time at which this nonphysical wavefront reaches that point.

Nonphysical event 2 occurs throughout the subsurface. It is caused by the crosscorrelation between the S-wave scattered data $G^{S(\Phi,\Phi)}_{(S,P)}(\mathbf{x}_R,\mathbf{x}_S)$ due to a conversion at the density perturbation and recorded at the receiver arrays, and the P-wave reference propagator $G^{0(\Phi,\Phi)}_{(P,P)}(\mathbf{x}_B,\mathbf{x}_R)$. Figure 6b explains the creation of this event for a point $\mathbf{x}_B$ located in region B using a stationary-phase approach.

Correctly combining velocity-stress recordings and quadrupole-dipole backpropagating sources is the key component to obtain a receiver wavefield deprived of the above two types of spurious events. Figure 7 shows how the scattered P-wavefield between a physical source and any point in the subsurface

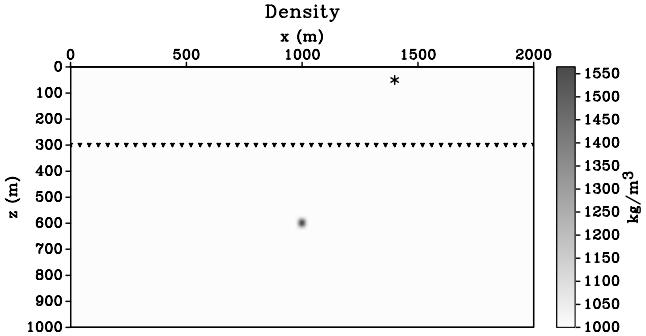

Figure 4. Elastic RTM geometry. A single point scatterer (gray spot in the density grid) is embedded in a homogeneous medium with velocities $v_P = 2600$ m/s, $v_S = 1400$ m/s, and density $\rho = 1000$ kg/m^3. The scatterer represents a positive density perturbation of $\Delta\rho = 600$ kg/m^3. The star indicates the location of a physical source, and every tenth receiver is marked by a triangle. Particle velocity recordings are injected at each receiver location in the wavefield extrapolation step.

$G^{S(\Phi,\Phi)}_{(M,P)}(\mathbf{x},\mathbf{x}_S)$ is created in equation 7 by summing the integral $\int_{\partial V}(G^{S(\tau,\Phi)}_{(ij,P)}(\mathbf{x}_R,\mathbf{x}_S)\{G^{0(\Phi,f)}_{(M,i)}(\mathbf{x},\mathbf{x}_R)\}^*)n_{R,j}d\mathbf{x}^2_R$ involving stress data and volume force density sources (Figure 7a) and the integral $\int_{\partial V}(G^{S(v,\Phi)}_{(i,P)}(\mathbf{x}_R,\mathbf{x}_S)\{G^{0(\Phi,h)}_{(M,ij)}(\mathbf{x},\mathbf{x}_R)\}^*)n_{R,j}d\mathbf{x}^2_R$ involving velocity data and deformation rate density sources (Figure 7b). The physically scattered P-waves share the same radiation pattern between the first and the second integrands, whereas the nonphysical waves have opposite polarity resulting in a perfect cancellation (other than small numerical errors due to the presence of dispersion in finite-difference data) when they are summed together (Figure 7c).

Consider now the region of the subsurface below the scatterer. Here, neither the tensorial nor the vectorial wavefield extrapolation construct the scattered P-wave traveling from the physical source to any image point $\mathbf{x}_C$ because the stationary receiver lies on a portion of the receiver boundary that is not available in a usual seismic experiment (Figure 6c). A comparison with the exact scattered P-wave in Figure 5 shows how both receiver wavefields share the same spurious event at early times (i.e., before the scattering event occurs) due to the crosscorrelation between the scattered P-wave and the reference P-wave propagator (Figure 5 — time 1 and Figure 6d). Furthermore, after the scattering event takes place (Figure 5 at times 2–5), the scattered P-wave appears to propagate only upward rather

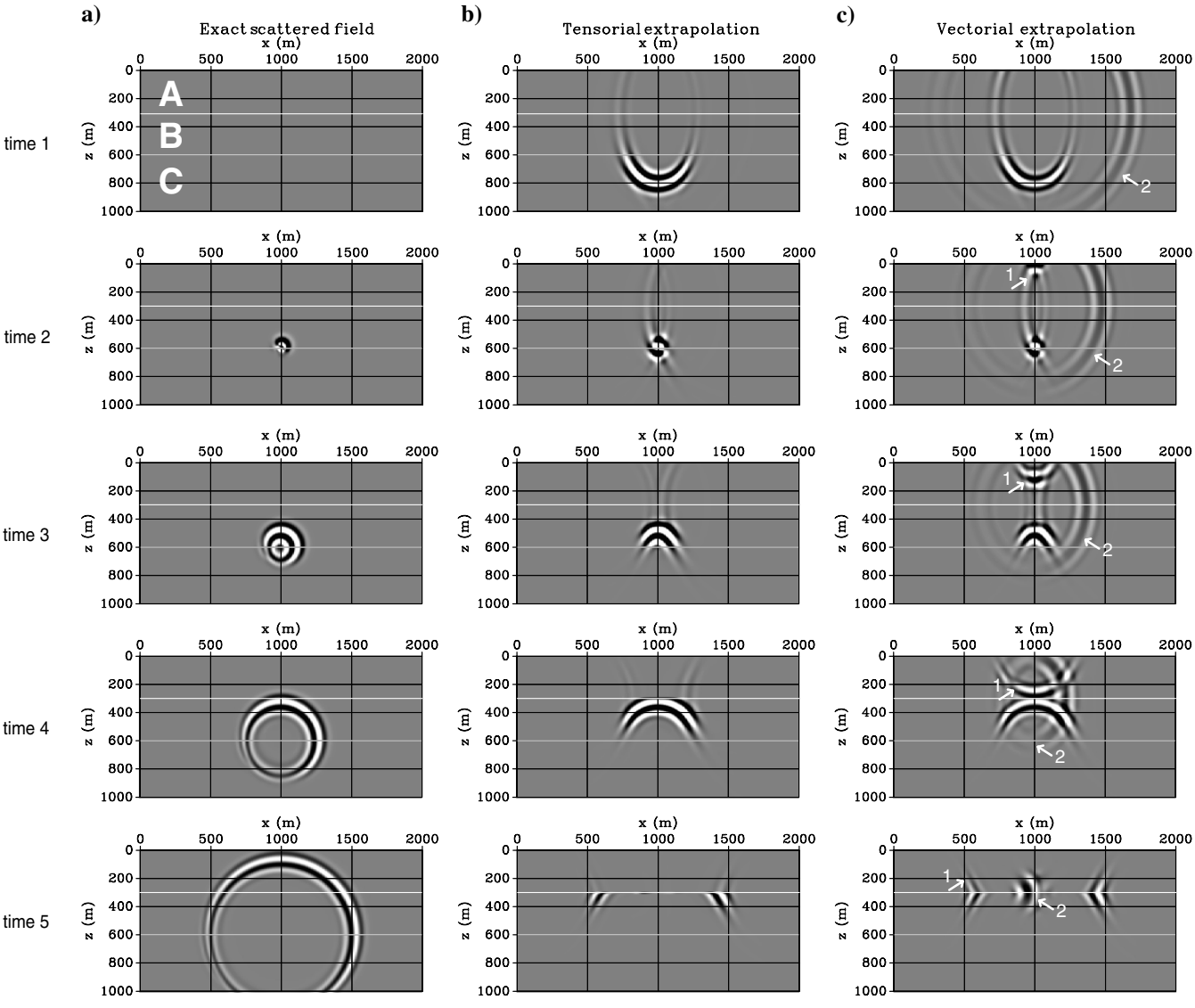

Figure 5. Series of snapshots of the (a) exactly modeled (b) tensorially, and (c) vectorially back-extrapolated receiver-side P-wavefield $\bar{G}^{S(\Phi,\Phi)}_{(P,P)}(\mathbf{x},\mathbf{x}_S)$ for the point scatterer example (Figure 4). Wavefields from the exact case (a) recorded at receivers in Figure 4 are injected at receiver locations in cases (b) and (c), and backpropagated toward earlier times (upward in this Figure). White lines at depths $z = z_R =$ 300 m and $z = z_{\text{scatt}} = 600$ m define the boundaries of three regions A, B, and C of the subsurface domain where the exact, vectorial, and tensorial receiver wavefields show different features. Particularly, white arrows indicate nonphysical waves due to approximations made in the vectorial wavefield extrapolation integral (equation 8); types 1 and 2 are explained in the text. These nonphysical waves do not arise when the exact wavefield extrapolation integral is carried out.

than "isotropically" in any direction (or in reverse time, the scattered P-wave collapsing onto the scatterer comes only from the direction of the receiver array). Although nonphysical events 1 and 2 pertain to using only elastic monopole sources and receivers, differences in the scattered P-wave between the exact scattered wavefield (Figure 5a) and the extrapolated receiver-side wavefields (Figure 5b and 5c) are due to the availability of only an incomplete (open) boundary of receivers. All of these observations are summarized in Table 2.

Imaging condition and artifacts.—Spurious events in receiver-side wavefield extrapolation potentially turn into artifacts in the final image. However, because an imaging condition often uses only the zero-time, zero-offset crosscorrelation between source and receiver wavefields, artifacts would only be created if the source wavefield and nonphysical waves in the receiver-side wavefield extrapolation coincide at the image point at a certain time. This is obviously not the case for nonphysical wavefield 1, which is due to the lack of directionality in the particle velocity injection because the source wavefield reaches any point $\mathbf{x}_A$ before the upward-injected P-wave. Moreover, absorbing boundary conditions are used at the top of the model in the extrapolation procedure to avoid the upgoing nonphysical wave being reflected back into the subsurface. On the other hand, because the source wavefield propagates from the source toward infinity and the nonphysical wavefield 2 starts from infinity and collapses at the receiver array (Figure 8), they inevitably cross at a certain time, creating artifacts in the PP image.

Figure 9 shows the PP images obtained from elastic RTM using the tensorial (Figure 9a) and vectorial (Figure 9b) wavefield extrapolation and the linearized imaging condition in equation 4. The scatterer is correctly imaged in both cases; however, a strong artifact is present when the vectorial receiver wavefield is crosscorrelated with the source wavefield (Figure 9b). This is caused by the use of only velocity data/volume force density sources in the receiver-side extrapolation. Because nonphysical wave 2 is not present in the tensorial receiver wavefield, the artifact is strongly attenuated in the final result in Figure 9a, creating a much clearer image, which allows a more accurate interpretation of the subsurface structure.

PS imaging

To evaluate an imaging condition for converted-waves (a so-called PS image) the computation of the S-wave receiver wavefield is required. In this section, we analyze the effect of using only particle velocity data to extrapolate the shear wavefield and describe how artifacts arise in the final image because of spurious events in the receiver-side extrapolation.

A series of snapshots of the S-wave receiver-side extrapolated field is compared to the exactly modeled scattered S-wave wavefield $\bar{G}^{S(\Phi,\Phi)}_{(S,P)}(\mathbf{x},\mathbf{x}_S)$ (Figure 10). Nonphysical wavefields 1 and 2 are explained similarly to those of the corresponding waves in the P-wave extrapolated wavefield. The main difference concerns the shape of spurious event 2 and the chronological order at which

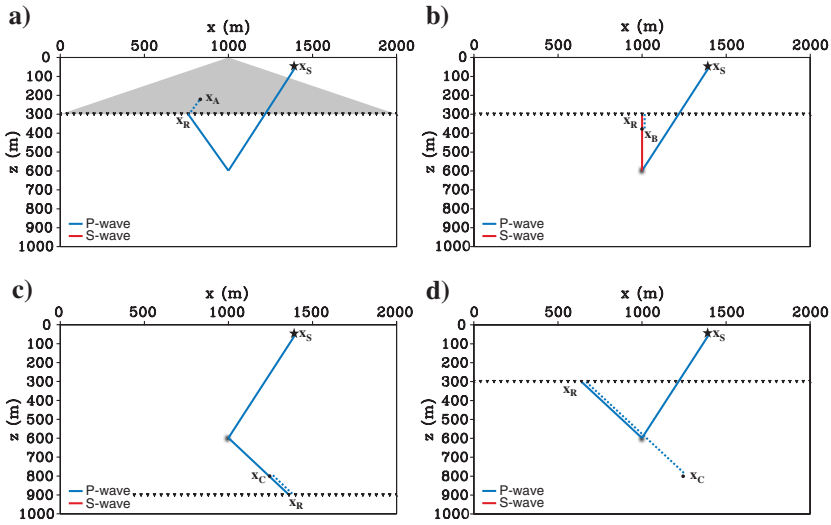

Figure 6. Stationary-phase analysis describing which receivers contribute to the construction of either physical or nonphysical energy in the receiver-side back-extrapolated wavefield. Solid lines represent the scattered Green's functions propagated forward in time during data acquisition and recorded on the receiver array. Dotted lines represent the reference Green's functions that are time reversed and injected at receiver location $\mathbf{x}_R$, propagating backwards in time during numerical back-extrapolation. Blue lines refer to P-waves, and red lines identify S-waves. (a) Nonphysical stationary path in the crosscorrelation of scattered P-wave data and the reference P-wave receiver-side propagator at $\mathbf{x}_A$. This event corresponds to an upgoing scattered P-wave, erroneously injected also as an upgoing time-reversed P-wave along the receiver array. (b) Nonphysical stationary path involved in the crosscorrelation of scattered S-wave data and the reference P-wave receiver-side propagator at $\mathbf{x}_B$. This event corresponds to a recorded scattered S-wave, erroneously injected as a P-wave along the receiver array. (c) Physical stationary path that would occur in the crosscorrelation of scattered P-wave data and the reference P-wave receiver-side propagator at $\mathbf{x}_C$; however, an array of receivers at depth $z > z_{\text{scatt}}$ is required to construct this physical event. (d) Nonphysical stationary paths in the crosscorrelation of scattered P-wave data and the reference P-wave receiver-side propagator at $\mathbf{x}_C$.

Table 2. Comparison between the vectorial (left of slash) and tensorial (right of slash) receiver-side back-extrapolated wavefields with respect to the three main events discussed in the text for three different regions of the subsurface domain: V, properly handled; X, improperly handled; and X/V, improperly handled by vectorial extrapolation but properly handled by tensorial extrapolation.

	Physical scattered wavefield	Nonphysical artifact (1)	Nonphysical artifact (2)
Region A ($z \le z_{\mathbf{r}}$)	—	X/V	X/V
Region B ($z_R < z \le z_{\text{scatt}}$)	V/V	—	X/V
Region C ($z > z_{\text{scatt}}$)	X/X	—	X/V

these waves collapse at the receiver array: Nonphysical wavefield 2 now arrives *before* the physical scattered S-wave. Wavefront 2, a scattered P-wave injected erroneously as an S-wave, has a parabolic shape: more precisely, two parabolic wavefronts propagate in opposite directions reaching the receiver array at the same time. Note that the wavefront indicated with the label "1 + 2" represents a recorded S-wave that was erroneously backpropagated as a P-wave, also in the wrong direction.

Figure 11 shows the source-side forward-propagating P-wave wavefield $G^{0(\Phi,\Phi)}_{(P,P)}(\mathbf{x},\mathbf{x}_S)$ (Figure 11a), and the tensorially (Figure 11b) and vectorially (Figure 11c) backpropagated S-wave receiver wavefields $\tilde{G}^{S(\Phi,\Phi)}_{(S,P)}(\mathbf{x},\mathbf{x}_S)$, which are crosscorrelated to evaluate the imaging condition in equation 4 (Figure 12). Artifact A1+2 in Figure 12b arises from the intersection of the source wavefield with the upper part of nonphysical wave 1 + 2, whereas artifact A2 is due to the lower part of spurious event 2 (Figure 11c).

Elastic RTM of the Marmousi 2 model

We now use a modified subset of the Marmousi 2 model (Martin et al., 2002) to compare the receiver-side extrapolation formulae in a more realistic scenario. Figure 13a depicts the stratigraphic density model composed of a series of layers with increasing dip toward the right side. The P- and S-wave velocity models used for migration are smooth with velocities ranging, respectively from 1.6 to 3.2 km/s and 0.8 to 1.6 km/s ($v_P/v_S = 2$) (Figure 13b). Data are modeled using density discontinuities to generate reflections, whereas we use a constant migration density throughout the model ($\rho = 10^{12}$ kg/km^3) to carry out Born imaging (i.e., for calculation of the source-side reference wavefield and for receiver-side back-propagation). A compressional source is fired at $\mathbf{x}_S = (6.75, 0.5)$ km, and the wavefields are recorded by a horizontal array of receivers placed at $z_R = 0.5$ km with inter-receiver spacing of $\Delta x_R = 2.5$ m. Absorbing boundary conditions are used for modeling and migration.

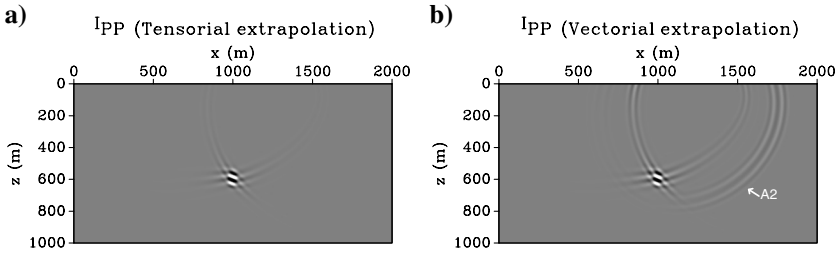

Figure 9. PP images resulting from elastic RTM using (a) tensorial and (b) vectorial wavefield extrapolation for the example in Figure 4 illuminated by a single surface source. Although the scatterer is correctly imaged in both cases (it can not be properly localized because only a single source was used in this example), artifact A2 is clearly visible below and to the right of the scatterer when only particle velocity data are injected at receiver locations during wavefield extrapolation. This results from the crosscorrelation between the source wavefield (Figure 8a) and nonphysical event 2 in the extrapolated receiver wavefield (Figure 8c).

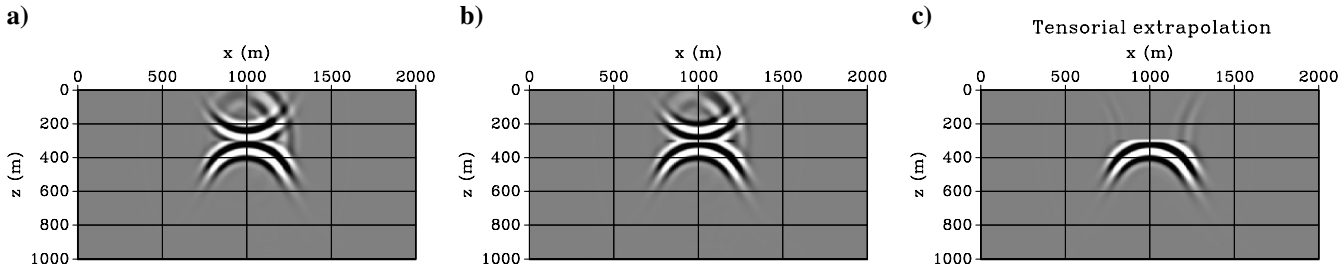

Figure 7. Construction of the correct back-extrapolated receiver-side P-wavefield using the tensorial wavefield extrapolation integral (equation 7) for the example in Figure 4: (a) first term, (b) second term, and (c) the sum of the integrals shown in (a) and (b). These wavefields share the same radiation pattern for the physical event (the downgoing scattered P-wave), whereas radiation patterns of the opposite sign cancel out in (c) for the nonphysical events (the upgoing scattered P-wave and the spurious P-wave due to the S-wave recorded at the receiver array).

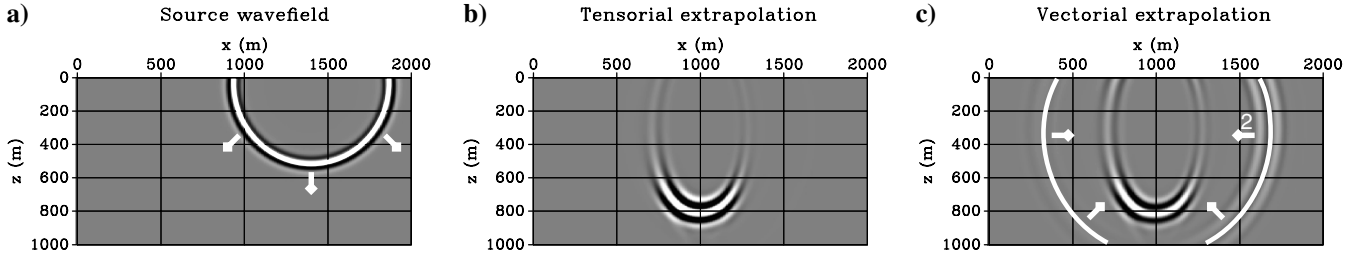

Figure 8. Time snapshot of (a) the source-side P-wave wavefield $G^{0(\Phi,\Phi)}_{(P,P)}(\mathbf{x},\mathbf{x}_S)$, and the (b) tensorial and (c) vectorial P-wave receiver-side back-extrapolated wavefields $\tilde{G}^{S(\Phi,\Phi)}_{(P,P)}(\mathbf{x},\mathbf{x}_S)$ for the example in Figure 4. The source wavefield is crosscorrelated with one of the receiver wavefields and the image is the value of the result at zero-time. This corresponds to the source wavefield snapshot being multiplied by the corresponding receiver wavefield (and the resulting panels at different times being summed together). In (a) the arrows identify the propagation direction of the source wavefield, and in (c) the arrows define propagation direction of non-physical event 2 in the vectorial receiver wavefield. Since they propagate in opposite directions and cross each other, they create an artifact in the final image (indicated in Figure 9b).

Receiver-side P- and S-wave extrapolated wavefields are computed using the tensorial (Figure 14a and 14c) and vectorial (Figure 14b and 14d) wavefield extrapolation integrals. The complexity of the model results in seismic data that are densely populated by events of every kind, ranging from primary reflected P-waves to primary converted S-waves and multiply scattered and converted P- and S-waves. When the vectorial expression is used for wavefield extrapolation, the number of wavefronts injected along the line of receivers is twice the number of physical waves reaching the earth's surface: a nonphysical S- or P-wave is erroneously generated from every physical P- or S-wave, respectively. In Figure 14b, several spurious waves, propagating transversally with respect to the physical ones, are indicated by white arrows: They mainly populate the right part of the model, although weak spurious energy is also visible on

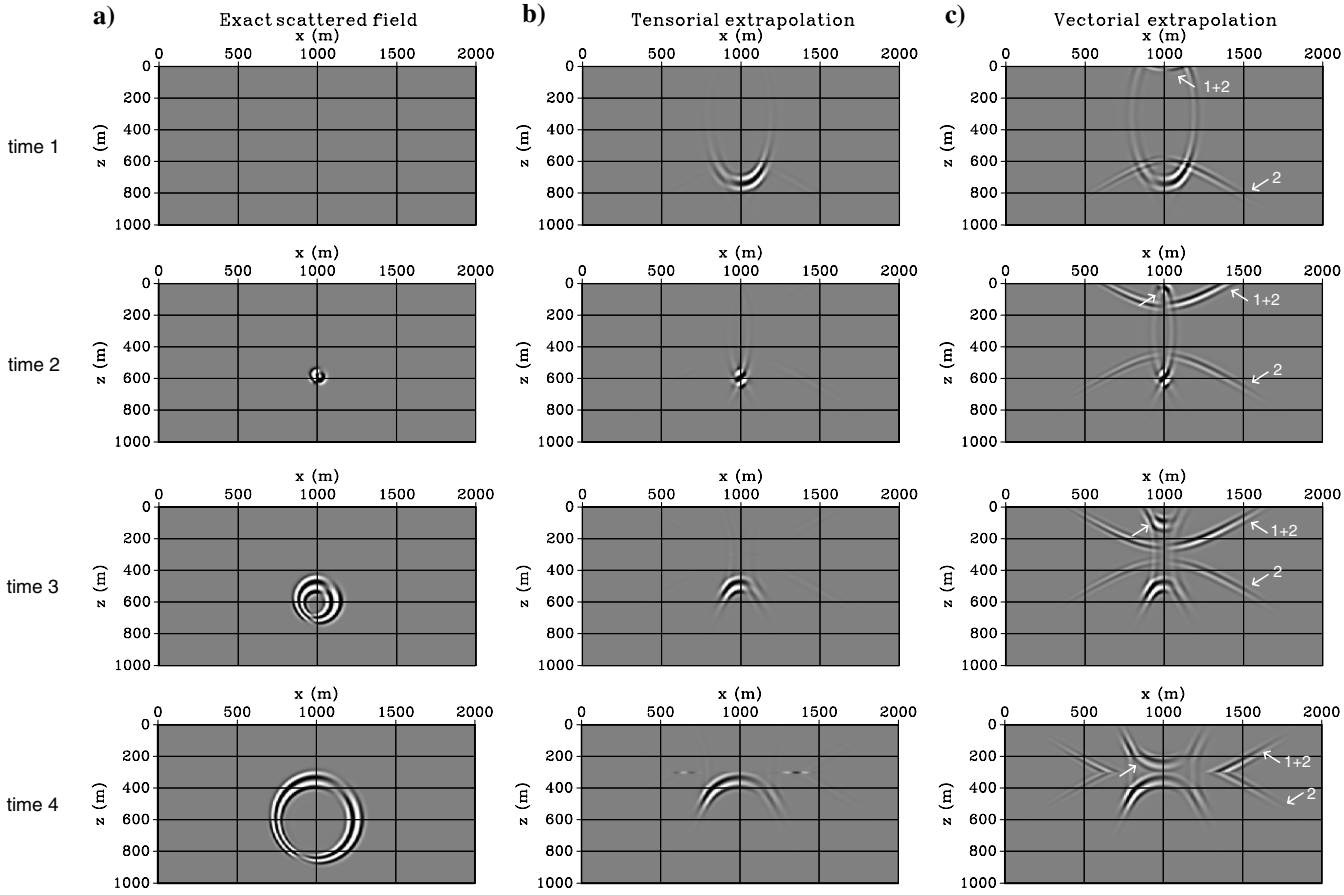

Figure 10. Series of snapshots of the (a) exactly modeled (b) tensorially and (c) vectorially back-extrapolated receiver-side S-wavefields $\bar{G}^{S(\Phi,\Phi)}_{(S,P)}(\mathbf{x},\mathbf{x}_S)$ for the point scatterer example (Figure 4). The white arrows indicate nonphysical waves due to approximations made in the wavefield extrapolation integral (equation 8). They do not arise (other than due to numerical artifacts) when the tensorial wavefield extrapolation integral is carried out in (b).

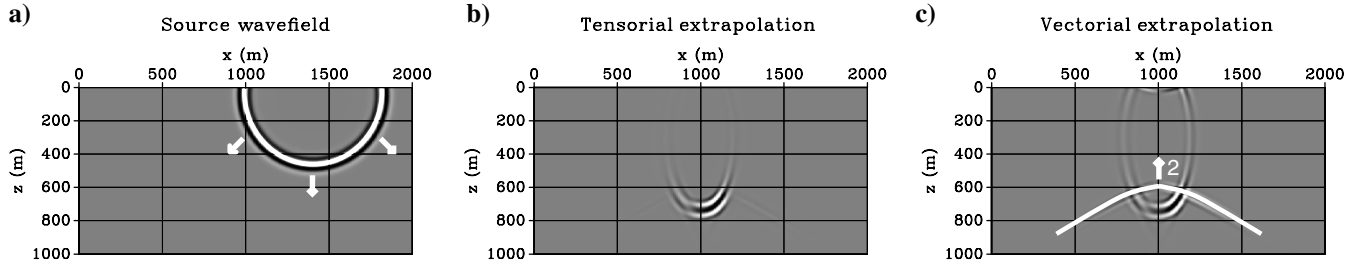

Figure 11. Time snapshot of (a) the source-side P-wave wavefield $G^{0(\Phi,\Phi)}_{(P,P)}(\mathbf{x},\mathbf{x}_S)$, and the (b) tensorial and (c) vectorial S-wave receiver-side back-extrapolated wavefields $\bar{G}^{S(\Phi,\Phi)}_{(S,P)}(\mathbf{x},\mathbf{x}_S)$ for the example in Figure 4. In (a) the arrows identify the propagation direction of the source wavefield and, in (c) the arrows define the propagation direction of non-physical event 2 in the vectorial receiver wavefield. They cross each other and create an artifact in the final image (Figure 12b).

the left side. Moreover, nonphysical events have an amplitude comparable with that of the physical events. On the other hand, the receiver-side S-wave wavefield (Figure 14d) seems to be less affected by nonphysical wavefronts, which propagate in a variety of different directions. The use of tensorial wavefield extrapolation integrals (Figure 14a and 14c) is necessary to generate receiver-side extrapolated wavefields deprived of artificial waves, whereas the backpropagated physical P- and S-wavefronts share the same kinematics as those obtained by the vectorial counterpart but are clearer and more discernible.

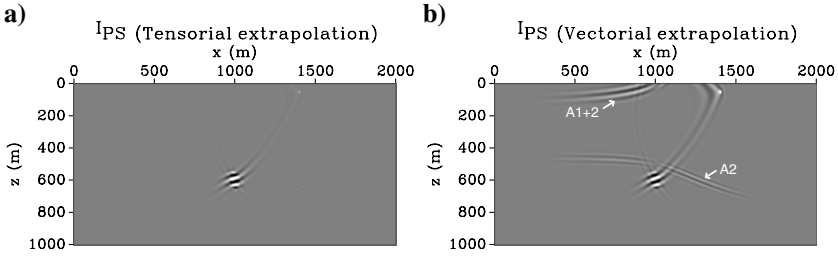

Figure 12. PS images resulting from elastic RTM using (a) tensorial and (b) vectorial wavefield extrapolation. Artifacts A1+2 and A2 are the result of the crosscorrelation between the P-wave source-side wavefield and spurious events in the S-wave receiver-side extrapolated wavefield when only particle velocity data are injected at the receiver locations during wavefield extrapolation.

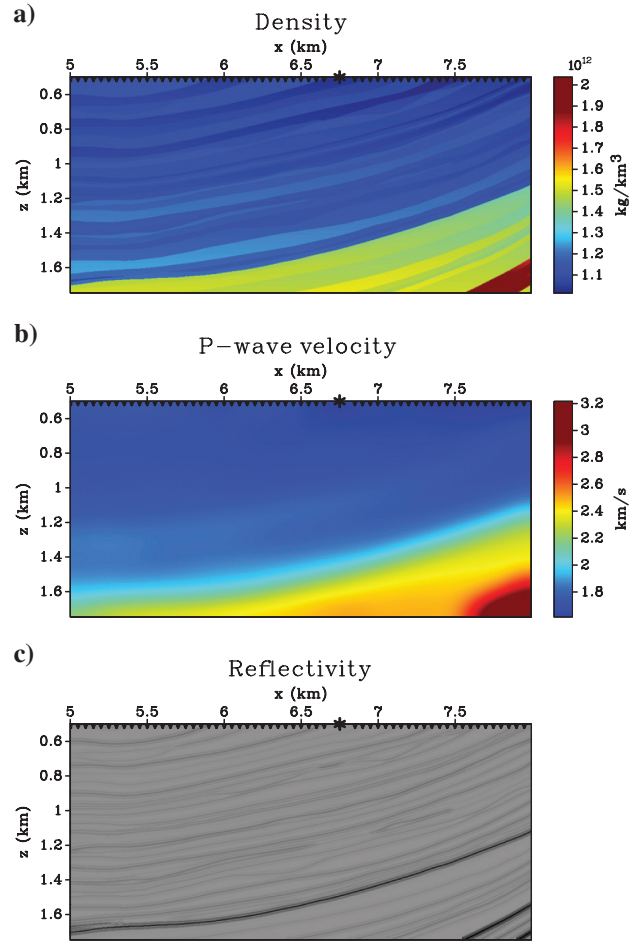

Figure 13. (a) Density model, (b) smoothed (migration) P-wave velocity, and (c) reflectivity ($r = |\nabla(\rho v_P)|$) models of a modified subset of the Marmousi 2 model (Martin et al., 2002) used for the third example of elastic RTM. The value of v_P ranges from 1.6 to 3.2 km/s and $v_P/v_S = 2a$; and the density ranges from 1 to 2 kg/km^3. The star indicates the location of the physical source, and every tenth receiver is marked by a triangle.

As a last step to produce PP and PS images of the subsurface, the linearized imaging condition (equation 4) is applied to the source- and receiver-side extrapolated wavefields (Figure 15). Spurious events in the receiver-side vectorial wavefields interfere with events in the source-side wavefields to generate artifacts in the final images. They distort the structure of the layered medium, especially in the near surface around coordinates $x = 7.25$ km and $z = 0.8$ km in the PP image (Figure 15b) and around coordinates $x = 6.75$ km and $z = 0.7$ km in the PS image (Figure 15d). A clear improvement is visible when using the receiver-side tensorial wavefields either for the PP image (Figure 15a) or the PS image (Figure 15c).

Ocean-bottom 4C data

We now demonstrate the seabed extrapolation formula (equation 11) by adding a water layer ($v_P = 1500$ m/s, $v_S = 0$ m/s, $\rho = 1000$ kg/m^3) on top of the Marmousi 2 model of Figure 13 to mimic an ocean-bottom imaging experiment. Synthetic data are computed using a source at $\mathbf{x}_S = (6.75, 0.005)$ km and a horizontal array of pressure and particle-velocity receivers placed along the seabed ($z_R = 0.5$ km). PP imaging using tensorial and vectorial wavefield backpropagation is performed below the receiver boundary (i.e., inside the elastic medium).

Data are initially modeled without free-surface multiples (i.e., with absorbing boundaries at the top of the water layer) to show the benefit arising from the correct injection of P- and S-waves. Figure 16 shows a time snapshot of the receiver-side P-wavefield computed using the tensorial and vectorial wavefield extrapolation integrals. In Figure 16b, analogously to Figure 14b, recorded S-waves are erroneously injected as P-waves and affect the vectorial wavefield (white arrows). PP images using tensorial (Figure 17a) and vectorial (Figure 17b) wavefield extrapolation are compared again showing the importance of using the pressure field along with the velocity recordings and the use of correct "injectors." A clear improvement by using tensorial extrapolation is visible throughout the model and especially in the shallower part, the vectorial artifacts being almost completely suppressed.

Lastly a free surface is added at the modeling stage, so that the recorded data are composed of up- and downgoing waves at the receiver array. The same time snapshots of the receiver-side P-wavefield as in Figure 16 are now displayed in Figure 18. Apart from the same nonphysical waves indicated by white arrows, some other artifacts appear in the vectorial wavefield (black arrows — Figure 18b): these are downgoing wavefields from multiples in the water layer, which are erroneously treated as upgoing recorded waves and are directly backpropagated downward into the subsurface. The tensorial extrapolation, on the other hand, accomplishes a

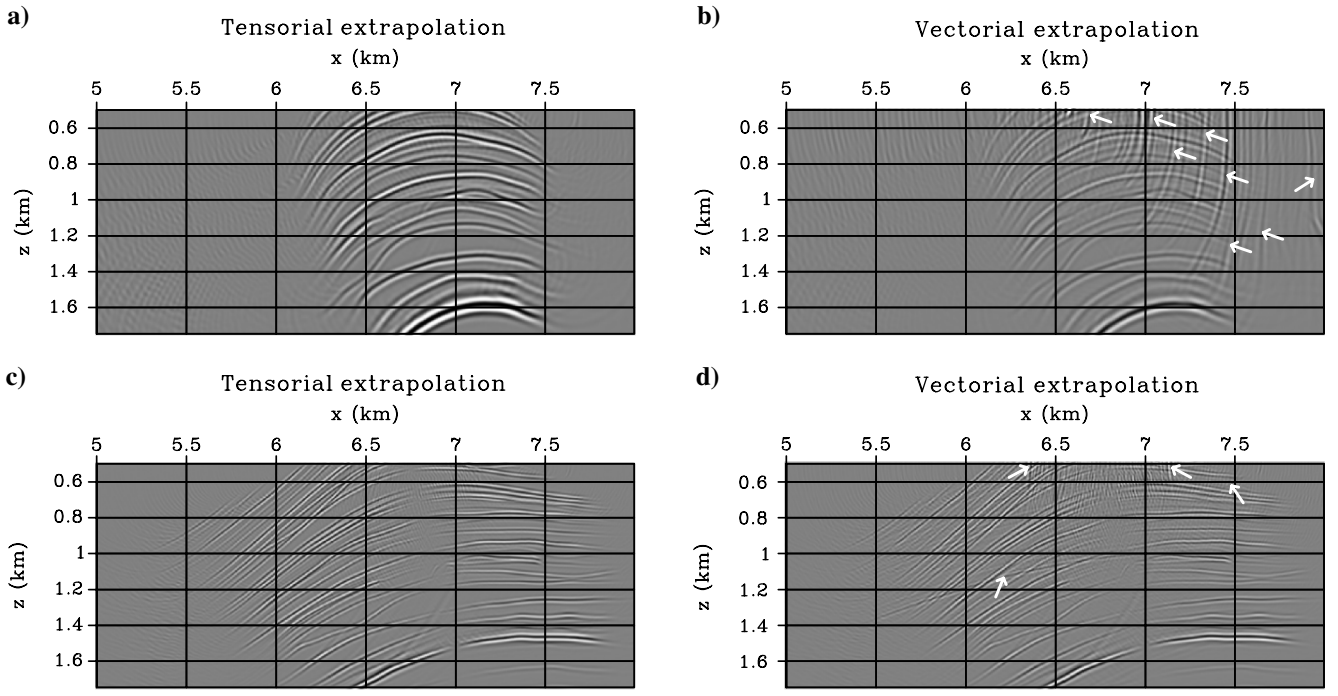

Figure 14. Comparison between a snapshot of the (a)/(c) tensorial, and (b)/(d) vectorial receiver-side back-extrapolated wavefields $\bar{G}^{S(\Phi,\Phi)}_{(P,P)}(\mathbf{x},\mathbf{x}_S)$ (top) and $\bar{G}^{S(\Phi,\Phi)}_{(S,P)}(\mathbf{x},\mathbf{x}_S)$ (bottom). White arrows show nonphysical waves of type 2 due to approximations made in the wavefield extrapolation integral in equation 8.

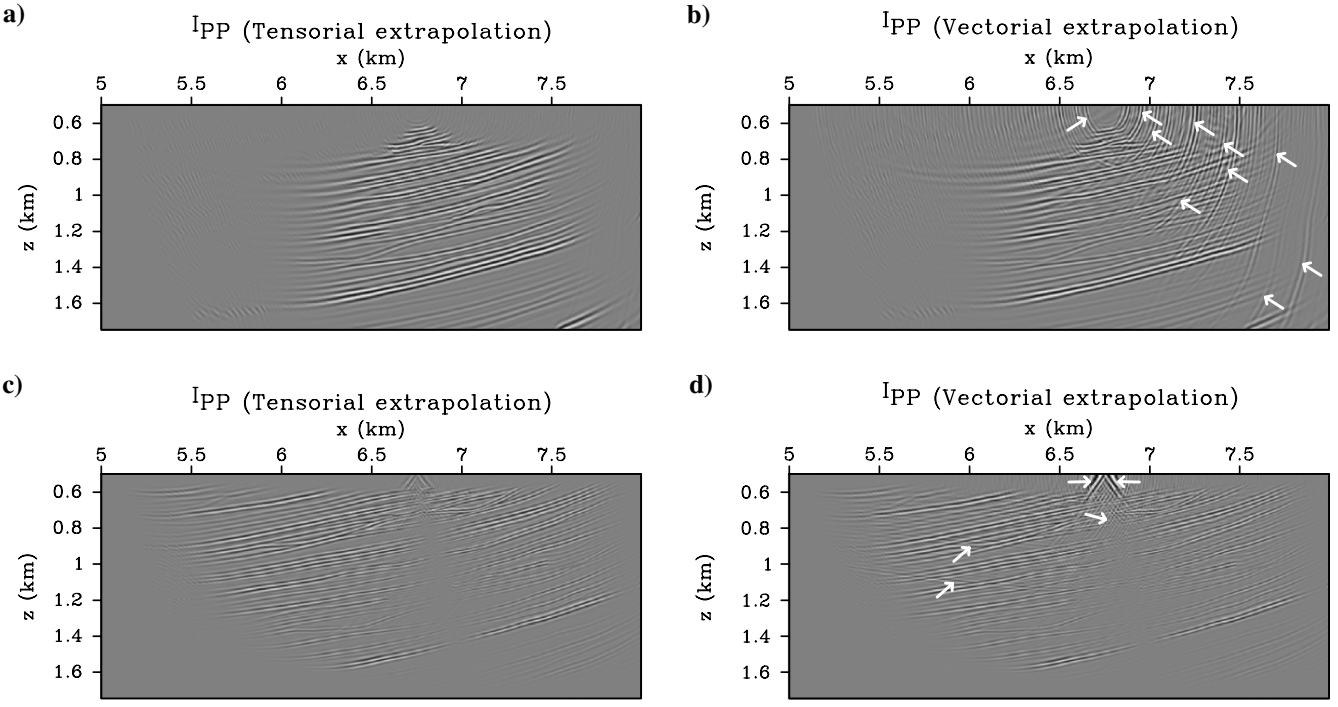

Figure 15. PP (top) and PS (bottom) images resulting from a single shot-profile elastic RTM of a modified subset of the Marmousi 2 model using the (a)/(c) tensorial and (b)/(d) vectorial wavefield extrapolation, respectively. Different portions of the subsurface domain are illuminated by pure- and converted-mode images because of different illumination angles of the two propagation modes for the given acquisition geometry. Nonphysical waves in the vectorial receiver-side extrapolated wavefield (Figure 14b and 14d) interfere with waves in the source wavefield to generate artifacts at the imaging stage (white arrows).

directional injection of the recorded wavefields and only upgoing waves are backpropagated inside the medium. Now, although the PP image constructed with the vectorial receiver wavefield (Figure 19b) shows further artifacts due to the interaction of the source wavefield with these downgoing waves injected in the opposite direction, the tensorial PP image (Figure 19a) is exactly the same as that obtained earlier by migrating *Born data* (Figure 17a). Hence, our tensorial extrapolation proves to be capable of separating the information from free-surface multiples (i.e., downgoing waves) from upgoing reflections when wavefields are injected.

DISCUSSION

Marine acquisition systems, which deploy receivers at the seabed (OBC or OBN) as an alternative to the more conventional marine streamer surveys, have created new potential but also new

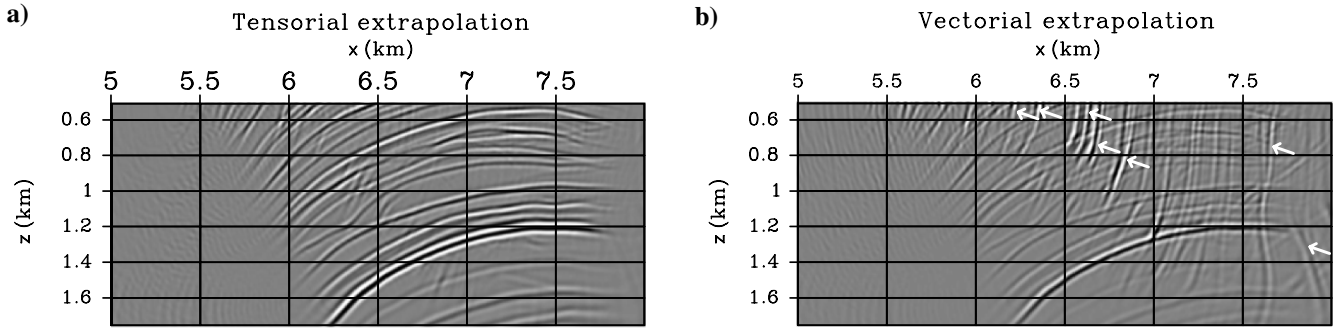

Figure 16. Comparison between a snapshot of the (a) tensorial and (b) vectorial P-wave receiver-side wavefields for the ocean-bottom example with absorbing boundaries at the top of the water layer (i.e., *Born data*). White arrows show nonphysical waves of type 2 due to approximations made in the wavefield extrapolation integral in equation 8.

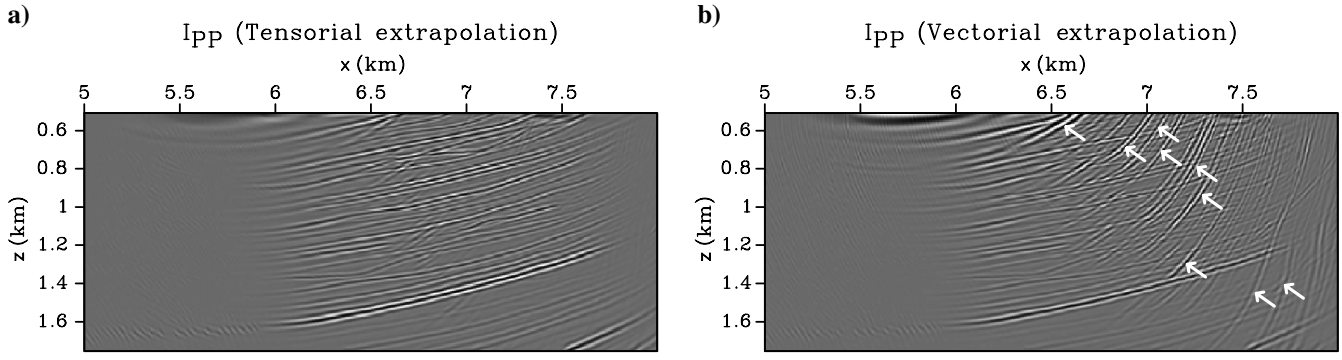

Figure 17. PP images resulting from a single shot-profile elastic RTM of an OBC version of the Marmousi 2 model (see main text) from data modeled with absorbing boundaries using (a) tensorial and (b) vectorial wavefield extrapolation, respectively. Nonphysical waves in the vectorial receiver-side back-extrapolated wavefield (Figure 16b) that interfere with waves in the source wavefield generate artifacts at the imaging stage (white arrows). These are successfully removed when tensorial wavefield extrapolation is used.

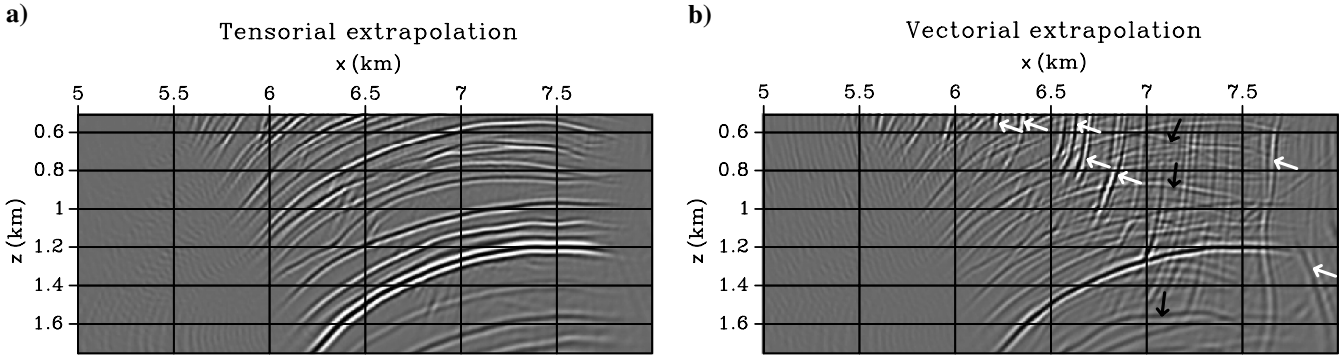

Figure 18. Comparison between a snapshot of the (a) tensorial and (b) vectorial P-wave receiver-side extrapolated wavefields for the ocean-bottom example with data modeled using a free surface. Black arrows show nonphysical waves of type 1, and white arrows show nonphysical waves of type 2.

processing and interpretation challenges. First, the acquisition geometry is very different from that of marine and land surveys: Sources and receivers are not located at approximately the same depth. Receiver depths range from tens of meters (shallow-water surveys) to hundreds of meters (deep-water surveys), and free-surface reflections modulate the spectrum more frequently than in marine streamer acquisition. Acquisition methods like over-under streamers (see Moldoveanu, 2007) and processing techniques like predictive deconvolution commonly used for the suppression of receiver-side ghosts, cannot easily be translated into this context. Second, because it is impossible to record shear waves when streamers are towed behind a vessel, multicomponent ocean-bottom data contain much more information about shear velocities and reflectivity because converted shear waves are recorded directly on horizontal component geophones at the seabed. A significant effort is needed, first, to reconcile this information with the P-wave data before the full potential of it can be exploited.

Having pressure information just above the seabed has been turned to an advantage for the separation of up- and downgoing (receiver-side ghost) waves using techniques such as "PZ summation" (Barr and Sanders, 1989; Soubaras, 1996; Schalkwijk et al., 1999); imaging using these separate components of the seismic data allows the reconstruction of the frequency band affected by the ghost notch effect (Godfrey et al., 1998; Grion et al., 2007; Dash et al., 2009). However, these additional data are often not used while performing migration, particularly during wavefield extrapolation: Receiver-side wavefields are generally obtained by backpropagation of particle velocity components at the receiver locations (Chang and McMechan, 1986, 1994; Sun and McMechan, 1986; Yan and Sava, 2008).

Here, we formulate an exact integral expression that uses a combination of velocity-stress recordings (or velocity-pressure in its application to ocean-bottom data — see above) and quadrupole-dipole backpropagating sources for wavefield extrapolation of elastic data. The numerical examples above show that direct injection of the particle displacement (or velocity) vector is not the best way to accomplish wavefield extrapolation, because it generates two types of nonphysical waves in the scattered wavefield estimate: Each arrival contained in the data is injected up- and downward, and all injected energy emits compressional and shear propagating modes. When using the tensorial integral expression for the extrapolation of the receiver-side wavefield, any wavefront is backpropagated only toward the direction from which it was traveling in the physical experiment, rather than up- and downward. Imaging of the primary signal (upgoing at the receiver array) and the ghost signal (downgoing at the receiver array) can therefore be accomplished without any preliminary up/down wavefield separation. In addition, injected energy emits only compressional or shear propagating modes (e.g., if a P-wave is recorded, only a P-wave mode is backpropagated), rather than both propagating modes as is the case for the usual backpropagation procedure. This is vital for imaging with elastic data because the improvement due to the proper focusing of singly and multiply converted waves is otherwise not realized due to the introduction of spurious events.

This new procedure has been proven to be effective for 2D imaging; however, it naturally extends to 3D if the Einstein's summation for repeated indices in equations 6 and 7 is carried out by considering an extra coordinate (i.e., x-y-z must be used instead of only x-z). Moreover, it is important to note that the cost of our tensorial extrapolation is identical to that of conventional vectorial extrapolation because velocity and stress data can be injected together in the modeling (finite-difference) code through deformation rate density and volume force density backpropagation sources, respectively.

A practical challenge presented by the application of the ocean-bottom tensorial extrapolation (equation 11) to data recorded along the seabed is the fact that backpropagation sources must be placed at the seabed, where a sharp change in the medium parameters occurs. We found that this caused a degradation in the cancellation of nonphysical waves in the tensorial wavefield extrapolation when an elastic finite-difference code is used. To alleviate this problem, we used a migration velocity/density model in which the elastic layer is upward continued to substitute for the sea layer (although in doing so we cannot take advantage of the wavefield separation property of the new extrapolation formula to perform imaging using the free-surface ghost along with the primaries). The explicit handling of the fluid-solid boundary condition in a finite-difference method (van Vossen et al., 2002) or the use of a finite or spectral-element modeling method (see Komatitsch and Tromp, 1999), in which the seabed properties in equation 10 can be represented explicitly at element boundaries, might solve this issue.

The imaging formulae in equations 1–4 are all (approximate) Green's functions for a colocated virtual, subsurface source and receiver at each image point. If the subsurface source and receiver are separated, the resulting Green's function would usually be referred to as an *extended* image (Sava and Vasconcelos, 2011). In

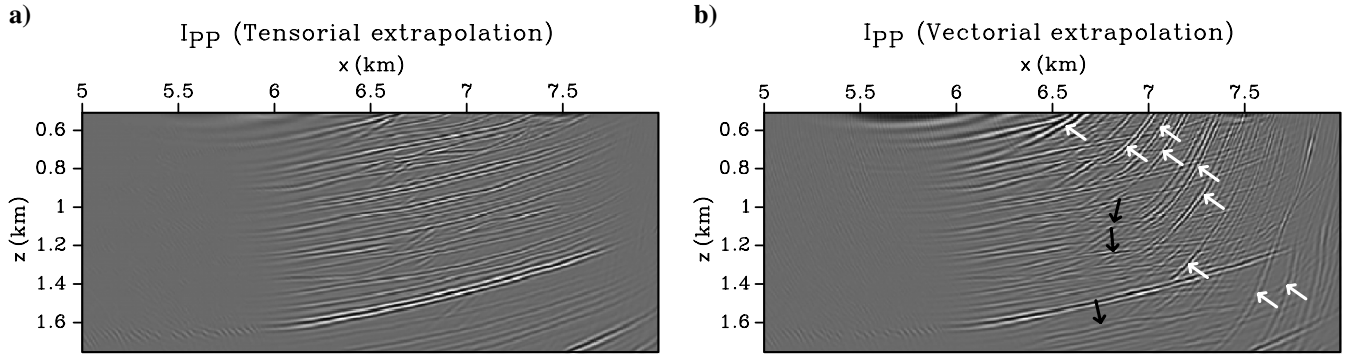

Figure 19. PP images resulting from a single shot-profile elastic RTM of an OBC version of the Marmousi 2 model from data modeled with a free surface using (a) tensorial and (b) vectorial wavefield extrapolation, respectively.

acoustic media, improvements in the receiver-side extrapolated wavefields not only result in better final images but also in more accurate extended images (Vasconcelos and Rickett, 2013), independently of the domain used for their computation, e.g., time-lag domain (Sava and Fomel, 2006), space-lag domain (Rickett and Sava, 2001), and angle domain (Sava and Fomel, 2003). Using our new extrapolation method, we would therefore expect similar improvements in elastic media. Moreover, because the penalty function usually defined for migration velocity analysis of elastic waves (Yan and Sava, 2010), which exploits the information contained in the extended images to invert for the velocity model, does not take into account the artificial events resulting from the vectorial extrapolation step, the inversion process could also benefit significantly from this new extrapolation procedure.

However, although our new wavefield extrapolation procedure improves the elastic image, the receiver wavefields still show some nonphysical waves at early times (e.g., before a scattering event occurs — see Figure 5c — time 1) and partial wavefronts at later times (e.g., after a scattering event occurs — see Figure 5c — times 3–5). These are caused first by the absence of nonlinear terms in the extrapolation and imaging steps and second by the lack of enclosing source and receiver boundaries as required by the theory of correlation-based extrapolation and imaging integrals. Note from a theoretical point of view that if both of these deficiencies would be resolved, all energy would focus on the correct locations (given a suitable velocity model, see below) and would then be correctly transferred back to the incident field and so would not be visible in the scattered field. That is, no energy would continue to propagate to other locations causing crosstalk. The reason is that equation 6 then gives exactly the true scattered Green's function, which is zero before the scattering events occur.

Equation 1 or equations 3 and 6 represent a framework suitable for a new, final stage of elastic imaging: Once we have a good estimate of the background model including high spatial frequencies (e.g., reflectors and diffractors) that introduce scattering in the back-propagation step, nonlinear terms can in principle be reintroduced to take advantage of the improved illumination offered by the energy from multiply scattered waves. These terms can alleviate illumination problems due to incomplete source and receiver aperture because the higher-order scattered waves come from a wider range of directions than primaries, as shown by Fleury and Snieder (2011) and Fleury and Vasconcelos (2012) for acoustic waves and by Ravasi and Curtis (2013) for elastic waves.

The lack of enclosing boundaries of sources/receivers has long presented challenges to the practice of seismic interferometry (Snieder et al., 2006; Wapenaar, 2006) and seismic imaging (see Lecomte, 2008). In seismic interferometry this limitation has been partly overcome by reformulating the Green's function retrieval problem as a multidimensional deconvolution (MDD) process using a convolution-type representation (Wapenaar et al., 2008, 2011; van der Neut et al., 2011). Unlike the correlation-type representation that holds only under the condition that the boundary is a closed surface, the convolution-type representation is valid for an open boundary as long as sources are on one side of (e.g., above) the boundary of receivers. Radiation conditions are then assumed to apply on the other half-space, closing the boundary by the assumption that the contribution of receivers on that part of the boundary will vanish (Wapenaar et al., 2011). Because seismic wavefield extrapolation also requires one source to lie outside of the integration domain, estimating the receiver-side wavefield by means of MDD could be beneficial, although an up-down separation would be additionally required because MDD deconvolves the downgoing wavefield from the upgoing wavefield. This topic will be the subject of further research.

CONCLUSION

In this work, we have derived a source-receiver interferometric framework for elastic imaging of land and ocean-bottom data. Reciprocity theorems are exploited to define a double integral formulation: A first integral representation is used for wavefield extrapolation of the scattered wavefield between a physical source and any image point (i.e., construction of the receiver-side wavefield), and a second identifies how source- and receiver-side wavefields must be combined by the imaging condition.

We show that tensorial wavefield extrapolation, which uses a combination of velocity-stress recordings and quadrupole-dipole backpropagating sources, generates receiver-side wavefields deprived of nonphysical waves that, by contrast, arise when wavefield extrapolation is approximated by direct injection of particle velocity components as dipole backpropagating sources at the receiver locations (vectorial wavefield extrapolation). Interfaces and layers are clearly discernible in synthetic elastic images of part of the Marmousi 2 model, even for the extreme case of RTM of a single shot gather.

In a marine scenario, under the fluid-solid interface boundary conditions which may hold on the seabed, we have also shown that the wavefield extrapolation integral turns into an expression that requires only pressure and particle velocity recordings. The latter are available from standard 4C seabed acquisition systems.

ACKNOWLEDGMENTS

The authors thank the Edinburgh Interferometry Project sponsors (ConocoPhillips, Schlumberger Cambridge Research, Statoil, and Total) for supporting this research. We are grateful to associate editor J. Schleicher, D. Draganov, D.-J. van Manen, and two other anonymous reviewers for their valuable comments that helped to improve the manuscript. The reproducible numerical examples in this work use the Madagascar open-source package freely available from http://www.reproducibility.org.

APPENDIX A

A RECIPROCAL SOURCE-RECEIVER FRAMEWORK FOR IMAGING OF OCEAN-BOTTOM DATA

Imaging with ocean-bottom multicomponent data can require the application of so-called *source-receiver reciprocity* (Wapenaar and Fokkema, 2006) to the theory provided in the main text. Sources usually define a roughly uniformly sampled portion of a boundary because they are fired at regular times along lines by a boat moving over the sea surface at constant speed. If data are acquired by OBNs, receivers may be significantly more sparsely and less uniformly spaced on the seabed.

The first step in a source-receiver imaging framework (wavefield extrapolation) requires the simultaneous injection of seismic data in a modeling code (e.g., finite-differences). To do so, a uniformly spaced boundary may be preferred because it aids error control

during preliminary data interpolation along the modeling grid. Applying source-receiver reciprocity, the boundary of sources can be used at this stage (Figure A-1b), and seismic data resorted into common-receiver gathers are backpropagated into the model from source positions. Once the extrapolated wavefield is estimated, the source wavelet is injected at any receiver location to create the forward-extrapolated wavefield and the imaging condition is computed to create an image of the subsurface (Figure A-1a).

An exact elastic imaging condition with velocity-stress receivers and monopole P- or S-wave virtual sources/receivers in the subsurface is given by

$$\begin{aligned} I^{ml}_{NM}(\mathbf{x}) &= 2\mathrm{Re}\{\Phi^{S(\Phi,\Phi)}_{(M,N)}(\mathbf{x}, t=0)\} \\ &= -\int\Bigg(\int_{\partial V_R}(\bar{G}^{S(\tau,\Phi)}_{(ij,N)}(\mathbf{x}_R,\mathbf{x})\{G^{0(v,\Phi)}_{(i,M)}(\mathbf{x}_R,\mathbf{x})\}^* \\ &\quad + \bar{G}^{S(v,\Phi)}_{(i,N)}(\mathbf{x}_R,\mathbf{x})\{G^{0(\tau,\Phi)}_{(ij,M)}(\mathbf{x}_R,\mathbf{x})\}^*)n_{R,j}d\mathbf{x}_R\Bigg)d\omega \\ &\quad -\int\Bigg(\int_{\partial V_R}(\bar{G}^{(\tau,\Phi)}_{(ij,N)}(\mathbf{x}_R,\mathbf{x})\{G^{S(v,\Phi)}_{(i,M)}(\mathbf{x}_R,\mathbf{x})\}^* \\ &\quad + \bar{G}^{(v,\Phi)}_{(i,N)}(\mathbf{x}_R,\mathbf{x})\{G^{S(\tau,\Phi)}_{(ij,M)}(\mathbf{x}_R,\mathbf{x})\}^*)n_{R,j}d\mathbf{x}_R\Bigg)d\omega. \end{aligned} \tag{A-1}$$

Because no assumption about the model on and outside of ∂V_R is made up to this point, the imaging condition in equation A-1 is correct for in- and outgoing waves at the receiver boundary. Primary and ghost signals are both properly focused at the image point.

However, when only monopole P-wave sources are available as in the imaging condition in equation 3, an approximated integral expression must be used for wavefield back-extrapolation by injection of the seismic data along the source array. The extrapolation of a Green's function between a P- or S-wave source fired virtually in the subsurface and a physical particle velocity receiver is

$$\begin{aligned} 2\mathrm{Re}\left\{\bar{G}^{S(v,\Phi)}_{(i,N)}(\mathbf{x}_R,\mathbf{x})\right\} \approx &\frac{2}{\rho c_P}\int_{\partial V_S}\{\bar{G}^{S(v,\Phi)}_{(i,P)}(\mathbf{x}_R,\mathbf{x}_S)\}^* G^{0(\Phi,\Phi)}_{(N,P)}(\mathbf{x},\mathbf{x}_S)d\mathbf{x}_S \\ &+\frac{2}{\rho c_P}\int_{\partial V_S}\{\bar{G}^{(v,\Phi)}_{(i,P)}(\mathbf{x}_R,\mathbf{x}_S)\}^* G^{S(\Phi,\Phi)}_{(N,P)}(\mathbf{x},\mathbf{x}_S)d\mathbf{x}_S, \end{aligned} \tag{A-2}$$

whereas the Green's function between a P- or S-wave virtually fired source in the subsurface and a physical stress receiver is

$$\begin{aligned} 2\mathrm{Re}\left\{\bar{G}^{S(\tau,\Phi)}_{(ij,N)}(\mathbf{x}_R,\mathbf{x})\right\} \approx &\frac{2}{\rho c_P}\int_{\partial V_S}\{\bar{G}^{S(\tau,\Phi)}_{(ij,P)}(\mathbf{x}_R,\mathbf{x}_S)\}^* G^{0(\Phi,\Phi)}_{(N,P)}(\mathbf{x},\mathbf{x}_S)d\mathbf{x}_S \\ &+\frac{2}{\rho c_P}\int_{\partial V_S}\{\bar{G}^{(\tau,\Phi)}_{(ij,P)}(\mathbf{x}_R,\mathbf{x}_S)\}^* G^{S(\Phi,\Phi)}_{(N,P)}(\mathbf{x},\mathbf{x}_S)d\mathbf{x}_S. \end{aligned} \tag{A-3}$$

The above approximations require that the model at and outside of ∂V_S is homogeneous, isotropic, and unperturbed. When this assumption is not satisfied in the recorded data (e.g., if source-side ghost and higher order multiples are not previously attenuated), the extrapolated wavefields will contain artificial events that erroneously crosscorrelate with the source-side wavefield to generate artifacts in elastic images.

APPENDIX B

RECIPROCITY-BASED TENSORIAL ELASTIC WAVEFIELD EXTRAPOLATION

An elastodynamic wavefield in a lossless arbitrarily inhomogeneous anisotropic solid medium is uniquely defined by the stress tensor $\tau_{ij}(\mathbf{x}, t)$ and the particle velocity $v_i(\mathbf{x}, t)$ at position $\mathbf{x}$ and time t (Aki and Richards, 1980; Snieder, 2002). In the space-frequency domain, the stress tensor and particle velocity obey the equation of motion

$$j\omega\rho v_i - \partial_j\tau_{ij} = f_i, \tag{B-1}$$

and we assume the linear stress-strain relation

$$-j\omega c_{ijkl}\tau_{kl} + (\partial_j v_i + \partial_i v_j)/2 = h_{ij}, \tag{B-2}$$

where $\rho(\mathbf{x})$ is the mass density of the medium, $c_{ijkl}(\mathbf{x})$ is the compliance (the stiffness $s_{ijkl}(\mathbf{x})$ is the inverse of the compliance), $f_i(\mathbf{x}, \omega)$ is the external volume force density, and $h_{ij}(\mathbf{x}, \omega)$ is the external deformation rate density. Given an interaction quantity that combines these quantities, Wapenaar and Fokkema (2006) identify the elastodynamic reciprocity theorem of the correlation type

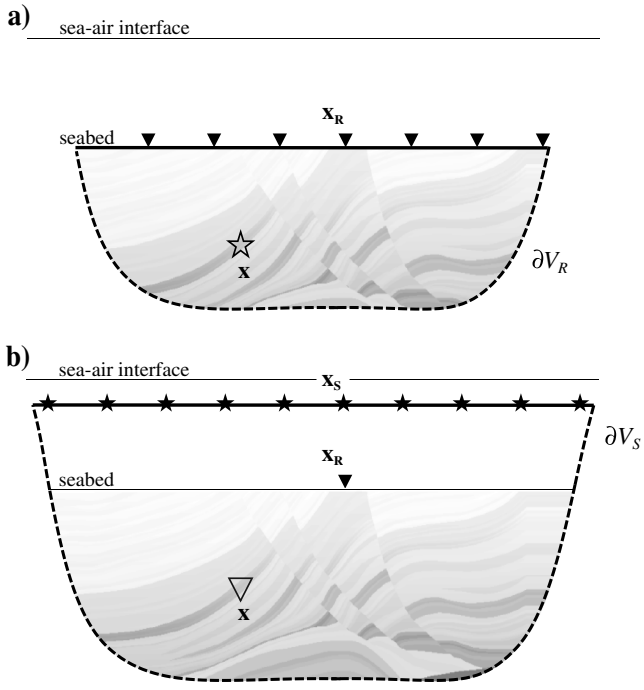

Figure A-1. Geometries used for the alternative version of reciprocity-based imaging condition and wavefield extrapolation. (a) A closed receiver boundary ∂V_R (receivers actually used in the acquisition are represented by triangles) is used at the imaging stage, whereas in (b) a closed source boundary ∂V_S (sources actually used in the acquisition are represented by stars) is used at the extrapolation stage.

$$\int_{V_R}\{-\tau^*_{ij,A}h_{ij,B}+v^*_{i,A}f_{i,B}-h^*_{ij,A}\tau_{ij,B}+f^*_{i,A}v_{i,B}\}d\mathbf{x}^3_R$$
$$=\oint_{\partial V_R}\{-v^*_{i,A}\tau_{ij,B}-\tau^*_{ij,A}v_{i,B}\}n_{R,j}d\mathbf{x}_R. \quad \text{(B-3)}$$

If impulsive point sources of force/deformation type and Green's functions are substituted for the wavefields in the elastodynamic reciprocity theorems, the reciprocity theorem of the correlation type leads to an elastodynamic Green's function representation theorem, which is the basis of seismic interferometry and of our tensorial wavefield extrapolation. Given the intersource geometry in Figure 2b with a physical source $\mathbf{x_S}$ located outside of a closed boundary of receivers ∂V_R that surrounds an imaginary source at the image point $\mathbf{x}$ in the subsurface (Slob et al., 2007), we obtain a Green's function representation using only point sources of force type

$$\bar{G}^{(v,f)}_{(m,k)}(\mathbf{x},\mathbf{x}_S)=-\int_{\partial V_R}(G^{(\tau,f)}_{(ij,k)}(\mathbf{x}_R,\mathbf{x}_S)\{G^{(v,f)}_{(i,m)}(\mathbf{x}_R,\mathbf{x})\}^*$$
$$+G^{(v,f)}_{(i,k)}(\mathbf{x}_R,\mathbf{x}_S)\{G^{(\tau,f)}_{(ij,m)}(\mathbf{x}_R,\mathbf{x})\}^*)n_{R,j}d\mathbf{x}_R. \quad \text{(B-4)}$$

Taking advantage of source-receiver reciprocity relations

$$G^{(v,f)}_{(i,m)}(\mathbf{x}_R,\mathbf{x})=G^{(v,f)}_{(m,i)}(\mathbf{x},\mathbf{x}_R),$$
$$G^{(\tau,f)}_{(ij,m)}(\mathbf{x}_R,\mathbf{x})=G^{(v,h)}_{(m,ij)}(\mathbf{x},\mathbf{x}_R), \quad \text{(B-5)}$$

an equivalent Green's function representation that mixes point sources of force and deformation types is obtained

$$\bar{G}^{(v,f)}_{(m,k)}(\mathbf{x},\mathbf{x}_S)=-\int_{\partial V_R}(G^{(\tau,f)}_{(ij,k)}(\mathbf{x}_R,\mathbf{x}_S)\{G^{(v,f)}_{(m,i)}(\mathbf{x},\mathbf{x}_R)\}^*$$
$$+G^{(v,f)}_{(i,k)}(\mathbf{x}_R,\mathbf{x}_S)\{G^{(v,h)}_{(m,ij)}(\mathbf{x},\mathbf{x}_R)\}^*)n_{R,j}d\mathbf{x}_R. \quad \text{(B-6)}$$

Equations B-4 and B-6 represent two alternative ways to construct the mth component of the particle velocity at $\mathbf{x}$ due to the kth component of an external volume force density source at $\mathbf{x_S}$. A boundary ∂V_R of receivers that record the full particle-velocity vector and stress tensor, and external volume force density source at $\mathbf{x}$ and $\mathbf{x_S}$, respectively, are required to evaluate equation B-4. Two colocated boundaries ∂V_R of sources and receivers that fire volume force density and deformation rate density sources and record the full particle velocity vector and stress tensor are instead required to evaluate equation B-6.

Equation B-4 looks more suitable for interferometric purposes because the requirements are less severe. This is not true when the Green's function between $\mathbf{x_S}$ and $\mathbf{x}$ has to be estimated in an imaging context. The terms $G^{(\tau,f)}_{(ij,k)}(\mathbf{x}_R,\mathbf{x}_S)$ and $G^{(v,f)}_{(i,k)}(\mathbf{x}_R,\mathbf{x}_S)$ represent the physical recording, and the terms $G^{(v,f)}_{(m,i)}(\mathbf{x},\mathbf{x}_R)$ and $G^{(v,h)}_{(m,ij)}(\mathbf{x},\mathbf{x}_R)$ are not recorded but may be computed numerically: they are the so-called propagators because they act on the recorded data and backpropagate them into the subsurface domain. The crosscorrelation and integration (sum) over receivers can be performed implicitly by injecting recorded data at all receivers simultaneously along a boundary of virtual sources (colocated with the boundary of physical receivers).

However, equation B-6 does not represent the scalar or vectorial potentials at the image point $\mathbf{x}$ originating from a P- or S-wave source at $\mathbf{x_S}$. These are needed to evaluate the second line of the nonlinear, reciprocity-based imaging condition in equation 3. Taking advantage of the P- and S-wave Green's functions defined by Wapenaar and Haimè (1990) and Wapenaar and Fokkema (2006), we recall that the P- and S-wave components of the wavefield can be expressed as a sum of partial derivatives of the velocities

$$G^{(\Phi,f)}_{(P,i)}=-\frac{\rho c_P^2}{j\omega}\partial_n G^{(v,f)}_{(m,i)},\quad G^{(\Phi,f)}_{(S_k,i)}=-\frac{\rho c_S^2}{j\omega}\varepsilon_{kjn}\partial_j G^{(v,f)}_{(m,i)}. \quad \text{(B-7)}$$

The wavefield extrapolation integral B-6 may then be recast as

$$\bar{G}^{(\Phi,\Phi)}_{(M,K)}(\mathbf{x},\mathbf{x}_S)=-\int_{\partial V_R}(G^{(\tau,\Phi)}_{(ij,K)}(\mathbf{x}_R,\mathbf{x}_S)\{G^{(\Phi,f)}_{(M,i)}(\mathbf{x},\mathbf{x}_R)\}^*$$
$$+G^{(v,\Phi)}_{(i,K)}(\mathbf{x}_R,\mathbf{x}_S)\{G^{(\Phi,h)}_{(M,ij)}(\mathbf{x},\mathbf{x}_R)\}^*)n_{R,j}d\mathbf{x}_R, \quad \text{(B-8)}$$

where we use the notation $\bar{G}^{(\Phi,\Phi)}_{(M,K)}(\mathbf{x},\mathbf{x}_S)$ to express the received P- or S-wave (M) recorded at point $\mathbf{x}$, due to a P- or S-wave source (K) located at $\mathbf{x_S}$.

To conclude, the nonlinear, reciprocity-based imaging condition in equation 3 requires also the scattered wavefield between a P- or S-wave source at $\mathbf{x_S}$ and a potential virtual receiver at the image point $\mathbf{x}$ (first line of equation 3). Following the approach that Wapenaar et al. (2010) propose, a generic Green's function can be written as the sum of reference and scattered wavefields ($G=G^0+G^S$) for any definition of the reference and scattered medium. Furthermore, because equation B-7 is still valid if any Green's function is substituted by the reference Green's function G^0 we obtain

$$\bar{G}^{0(\Phi,\Phi)}_{(M,K)}(\mathbf{x},\mathbf{x}_S)=-\int_{\partial V_R}(G^{0(\tau,\Phi)}_{(ij,K)}(\mathbf{x}_R,\mathbf{x}_S)\{G^{0(\Phi,f)}_{(M,i)}(\mathbf{x},\mathbf{x}_R)\}^*$$
$$+G^{0(v,\Phi)}_{(i,K)}(\mathbf{x}_R,\mathbf{x}_S)\{G^{0(\Phi,h)}_{(M,ij)}(\mathbf{x},\mathbf{x}_R)\}^*)n_{R,j}d\mathbf{x}_R. \quad \text{(B-9)}$$

Subtracting equation B-9 from B-8, we obtain the wavefield extrapolation integral in equation 5.

REFERENCES

Aki, K., and P. G. Richards, 1980, Quantitative seismology: W. H. Freeman & Co..

Amal, R., N. Bertram, and D. Herron, 2005, An experimental nodal OBS acquisition from the Thunder Horse Field, Gulf of Mexico: The Leading Edge, **24**, 410–412, doi: 10.1190/1.1901395.

Amundsen, L., 2001, Elimination of free-surface related multiples without need of a source wavelet: Geophysics, **66**, 327–341, doi: 10.1190/1.1444912.

Barr, F. J., and J. I. Sanders, 1989, Attenuation of water-column multiples using pressure and velocity detectors in a water-bottom cable: 59th Annual International Meeting, SEG, Expanded Abstracts, 653–656.

Berg, E., B. Svenning, and J. Martin, 1994, SUMIC — A new strategic tool for exploration and reservoir mapping: 56th Annual International Conference and Exhibition, EAGE, Extended Abstracts, G055.

Chang, W. F., and G. A. McMechan, 1986, Reverse-time migration of offset vertical seismic profiling data using the excitation-time imaging condition: Geophysics, **51**, 67–84, doi: 10.1190/1.1442041.

Chang, W. F., and G. A. McMechan, 1994, 3-D elastic prestack, reverse-time depth migration: Geophysics, **59**, 597–609, doi: 10.1190/1.1443620.

Curtis, A., and D. Halliday, 2010, Source-receiver wave field interferometry: Physical Review E, **81**, no. 4, 046601, doi: 10.1103/PhysRevE.81.046601.

Curtis, A., and J. O. A. Robertsson, 2002, Volumetric wavefield recording and near-receiver group velocity estimation for land seismics: Geophysics, **67**, 1602–1611, doi: 10.1190/1.1512751.

Dash, R., G. Spence, R. Hyndman, S. Grion, Y. Wang, and S. Ronen, 2009, Wide-area imaging from OBS multiples: Geophysics, **74**, no. 6, Q41–Q47, doi: 10.1190/1.3223623.

Fleury, C., and R. Snieder, 2011, Reverse-time-migration of multiply scattered seismic waves: 81st Annual International Meeting, SEG, Expanded Abstracts, 3382.

Fleury, C., and I. Vasconcelos, 2012, Imaging condition for nonlinear scattering-based imaging: Estimate of power loss in scattering: Geophysics, **77**, no. 1, S1–S18, doi: 10.1190/geo2011-0135.1.

Gaiser, J., N. Moldoveanu, C. Macbeth, R. Michelena, and S. Spitz, 2001, Multicomponent technology: The players, problems, applications, and trends: Summary of the workshop sessions: The Leading Edge, **20**, 974–977, doi: 10.1190/1.1487318.

Godfrey, R., P. Kristiansen, B. Armstrong, M. Cooper, and E. Thorogood, 1998, Imaging the Foinaven ghost: 68th Annual International Meeting, SEG, Expanded Abstracts, 1333–1335.

Granger, P. Y., M. Manin, J. L. Boelle, E. Ceragioli, F. Lefeuvre, and E. Crouzy, 2005, Autonomous 4C nodes used in infill areas to complement streamer data, deepwater case study: 75th Annual International Meeting, SEG, Expanded Abstracts, 84–87.

Grion, S., R. Exley, M. Manin, X. Miao, A. Pica, Y. Wang, P. Granger, and S. Ronen, 2007, Mirror imaging of OBS data: First Break, **25**, 37–42, doi: 10.3997/1365-2397.2007028.

Halliday, D., and A. Curtis, 2010, An interferometric theory of source-receiver scattering and imaging: Geophysics, **75**, no. 6, SA95–SA103, doi: 10.1190/1.3486453.

Hughes, P., O. H. Hatland, J. M. Haynes, M. Øygaren, and G. Drivenes, 2010, De-risking a Palaeocene amplitude anomaly prospect using multi component seismic and controlled source electromagnetics: NPF Biennial Geophysical Seminar, Expanded Abstracts.

Knapp, S., N. Payne, and T. Johns, 2001, Imaging through gas clouds: A case history from the Gulf of Mexico: 71st Annual International Meeting, SEG, Expanded Abstracts, 776–779.

Komatitsch, D., and J. Tromp, 1999, Introduction to the spectral-element method for 3-D seismic wave propagation: Geophysical Journal International, **139**, 806–822, doi: 10.1046/j.1365-246x.1999.00967.x.

Lecomte, I., 2008, Resolution and illumination analyses in PSDM: A ray-based approach: The Leading Edge, **27**, 650–663, doi: 10.1190/1.2919584.

Leiceaga, G. G., J. Silva, F. Artola, E. Marquez, and J. Vanzeler, 2010, Enhanced density estimation from prestack inversion of multicomponent seismic data: The Leading Edge, **29**, 1220–1226, doi: 10.1190/1.3496912.

Li, X.-Y., 1998, Fracture detection using P-P and P-S waves in multicomponent sea-floor data: 68th Annual International Meeting, SEG, Expanded Abstracts, 2056–2059.

Martin, G. S., K. J. Marfurt, and S. Larsen, 2002, Marmousi-2: An updated model for the investigation of AVO in structurally complex areas: 72nd Annual International Meeting, SEG, Expanded Abstracts, 1979–1982.

Maver, K. G., 2011, Ocean bottom seismic: Strategic technology for the oil industry: First Break, **29**, 75–80.

Moldoveanu, N., L. Combee, M. Egan, G. Hampson, L. Sydora, and W. Abriel, 2007, Over/under towed streamer acquisition: A method to extend seismic bandwidth to both higher and lower frequencies: The Leading Edge, **26**, 41–58, doi: 10.1190/1.2431831.

Muijs, R., J. O. A. Robertsson, and K. Holliger, 2007, Prestack depth migration of primary and surface-related multiple reflections: Part I — Imaging: Geophysics, **72**, no. 2, S59–S69, doi: 10.1190/1.2422796.

Ravasi, M., and A. Curtis, 2013, Nonlinear scattering based imaging in elastic media: Theory, theorems and imaging conditions: Geophysics, **78**, no. 3, S137–S155, doi: 10.1190/geo2012-0286.1.

Rickett, J., and P. Sava, 2001, Offset and angle domain common-image gathers for shot-profile migration: 71st Annual International Meeting, SEG, Expanded Abstracts, 1115–1118.

Robertsson, J. O. A., and A. Curtis, 2002, Wavefield separation using densely deployed, three component, single sensor groups in land surface seismic recordings: Geophysics, **67**, 1624–1633, doi: 10.1190/1.1512809.

Robertsson, J. O. A., and E. Muyzert, 1999, Wavefield separation using a volume distribution of three component recordings: Geophysical Research Letters, **26**, 2821–2824, doi: 10.1029/1999GL010472.

Ronen, S., A. Ratcliffe, P. Nicholls, K. Mills, R. Leggott, K. Hawkins, and L. Scott, 2003, Combined ocean bottom stations and surface-towed seismic streamers: 65th EAGE Conference & Exhibition.

Ronen, S., L. Comeaux, and J. Miao, 2005, Imaging downgoing waves from ocean bottom stations: 75th Annual International Meeting, SEG, Expanded Abstracts, 963–966.

Sava, P., and S. Fomel, 2003, Angle-domain common-image gathers by wavefield continuation methods: Geophysics, **68**, 1065–1074, doi: 10.1190/1.1581078.

Sava, P., and S. Fomel, 2006, Time-shift imaging condition in seismic migration: Geophysics, **71**, no. 6, S209–S217, doi: 10.1190/1.2338824.

Sava, P., and I. Vasconcelos, 2011, Extended imaging condition for wave-equation migration: Geophysical Prospecting, **59**, 35–55, doi: 10.1111/j.1365-2478.2010.00888.x.

Schalkwijk, K. M., C. P. A. Wapenaar, and D. J. Verschuur, 1999, Application of two-step decomposition to multicomponent ocean-bottom data: Theory and case study: Journal of Seismic Exploration, **8**, 261–278.

Shahraeeni, M., and A. Curtis, 2011, Fast probabilistic nonlinear petrophysical inversion: Geophysics, **76**, no. 2, E45–E58, doi: 10.1190/1.3540628.

Shahraeeni, M., A. Curtis, and G. Chao, 2012, Fast probabilistic petrophysical mapping of reservoirs from 3D seismic data: Geophysics, **77**, no. 3, O1–O19, doi: 10.1190/geo2011-0340.1.

Simmons, J., and M. Backus, 2003, An introduction — Multicomponent: The Leading Edge, **22**, 1227–1262, doi: 10.1190/tle22121227.1.

Slob, E., D. Draganov, and K. Wapenaar, 2007, Interferometric electromagnetic Green's functions representations using propagation invariants: Geophysical Journal International, **169**, 60–80, doi: 10.1111/j.1365-246X.2006.03296.x.

Snieder, R., 2002, Scattering and inverse scattering in pure and applied science: Academic Press, Inc.

Snieder, R., 2004, Extracting the Green's function from the correlation of coda waves: A derivation: Physical Review E, **69**, 046610.

Snieder, R., K. Wapenaar, and K. Lerner, 2006, Spurious multiples in seismic interferometry of primaries: Geophysics, **71**, no. 4, SI111–SI124, doi: 10.1190/1.2211507.

Sonneland, L., and L. Berg, 1987, Comparison of two approaches to water layer multiple attenuation by wave field extrapolation: 57th Annual International Meeting, SEG, Expanded Abstracts, 276–277.

Soubaras, R., 1996, Ocean-bottom hydrophone and geophone processing: 66th Annual International Meeting, SEG, Expanded Abstracts, 24–27.

Stewart, R. R., J. E. Gaiser, R. J. Brown, and D. C. Lawton, 2003, Converted-wave seismic exploration: Applications: Geophysics, **68**, 40–57, doi: 10.1190/1.1543193.

Sun, R., and G. A. McMechan, 1986, Pre-stack reverse-time migration for elastic waves with application to synthetic offset vertical seismic profiles: Proceedings of the IEEE, **74**, 457–465, doi: 10.1109/PROC.1986.13486.

Thomsen, L., O. Barkved, B. Haggard, J. Kommedal, and B. Rosland, 1997, Converted-wave imaging of Valhall reservoir: 59th Annual International Conference and Exhibition, EAGE, B048.

van der Neut, J., J. Thorbecke, K. Mehta, E. Slob, and K. Wapenaar, 2011, Controlled-source interferometric redatuming by crosscorrelation and multidimensional deconvolution in elastic media: Geophysics, **76**, no. 4, SA63–SA76.

van Vossen, R., J. O. A. Robertsson, and C. H. Chapman, 2002, Finite-difference modeling of wave propagation in a fluid-solid configuration: Geophysics, **67**, 618–624, doi: 10.1190/1.1468623.

Vasconcelos, I., 2011, Source-receiver reverse-time imaging of vector-acoustic seismic data: 81st Annual International Meeting, SEG, Expanded Abstracts, 3184–3189.

Vasconcelos, I., 2013, Source-receiver reverse-time imaging of dual-source, vector-acoustic seismic data: Geophysics, **78**, no. 2, WA147–WA158, doi: 10.1190/geo2012-0475.1.

Vasconcelos, I., and J. Rickett, 2013, Broadband extended images by joint inversion of multiple blended wavefields: Geophysics, **78**, no. 2, WA123–WA145, doi: 10.1190/geo2012-0300.1.

Virieux, J., 1986, P-SV wave propagation in heterogeneous media: Velocity-stress finite-difference method: Geophysics, **51**, 889–901, doi: 10.1190/1.1442147.

Wang, Y., S. Grion, and R. Bale, 2009, What comes up must have gone down: The principle and application of up-down deconvolution for multiple attenuation of ocean bottom data: CSEG Recorder.

Wapenaar, K., 2006, Green's function retrieval by cross-correlation in case of one-sided illumination: Geophysics, **71**, no. 4, SI33–SI46, doi: 10.1190/1.2213955.

Wapenaar, K., and J. Fokkema, 2006, Green's function representations for seismic interferometry: Geophysical Research Letters, **33**, L19304, doi: 10.1029/2006GL027747.

Wapenaar, C. P. A., and G. C. Haimé, 1990, Elastic extrapolation of primary seismic P- and S-waves: Geophysical Prospecting, **38**, 23–60.

Wapenaar, K., E. Slob, and R. Snieder, 2008, Seismic and electromagnetic controlled-source interferometry in dissipative media: Geophysical Prospecting, **56**, 419–434, doi: 10.1111/j.1365-2478.2007.00686.x.

Wapenaar, K., E. Slob, and R. Snieder, 2010, On seismic interferometry, the generalized optical theorem, and the scattering matrix of a point scatterer: Geophysics, **75**, no. 3, SA27–SA35, doi: 10.1190/1.3374359.

Wapenaar, K., J. van der Neut, E. Ruigrok, D. Draganov, J. Hunziker, E. Slob, J. Thorbecke, and R. Snieder, 2011, Seismic interferometry by crosscorrelation and by multidimensional deconvolution: A systematic comparison: Geophysical Journal International, **185**, 1335–1364, doi: 10.1111/j.1365-246X.2011.05007.x.

Wong, M., B. Biondi, and S. Ronen, 2010, Joint least-squares inversion of up- and down-going signal for ocean bottom data sets: 80th Annual International Meeting, SEG, Expanded Abstracts, 2752–2756.

Wong, M., B. Biondi, and S. Ronen, 2011, Least-squares reverse time migration/inversion for ocean bottom data: A case study: 81st Annual International Meeting, SEG, Expanded Abstracts, 2369–2373.

Yan, J., and P. Sava, 2007, Elastic wavefield imaging with scalar and vector potentials: 77th Annual International Meeting, SEG, Expanded Abstracts, 2150–2154.

Yan, J., and P. Sava, 2008, Isotropic angle-domain elastic reverse-time migration: Geophysics, **73**, no. 6, S229–S239, doi: 10.1190/1.2981241.

Yan, J., and P. Sava, 2010, Analysis of converted-wave extended images for migration velocity analysis: 80th Annual International Meeting, SEG, Expanded Abstracts, 1666–1671.

Yilmaz, O., 1989, Seismic data processing: SEG.

Zhu, X., S. Altan, and J. Li, 1999, Recent advances in multicomponent processing: The Leading Edge, **18**, 1283–1288, doi: 10.1190/1.1438200.